Biomaterials Advances 134 (2022) 112721

Contents lists available at ScienceDirect

Biomaterials Advances

journal homepage: www.elsevier.com/locate/bioadv

Bilayered laponite/alginate-poly(acrylamide) composite hydrogel for osteochondral injuries enhances macrophage polarization: An *in vivo* study

Ecem Saygili [a], Pelin Saglam-Metiner [a], Betul Cakmak [a], Emine Alarcin [b], Goze Beceren [a], Pinar Tulum [a], Yong-Woo Kim [c,d], Kasim Gunes [e], Guler Gamze Eren-Ozcan [f], Dilek Akakin [e], Jeong-Yun Sun [c,d], Ozlem Yesil-Celiktas [a,*]

[a] Department of Bioengineering, Faculty of Engineering, Ege University, 35100 Izmir, Turkey
[b] Department of Pharmaceutical Technology, Faculty of Pharmacy, Marmara University, 34854 Istanbul, Turkey
[c] Department of Materials Science and Engineering, Seoul National University, 08826 Seoul, Republic of Korea
[d] Research Institute of Advanced Materials (RIAM), Seoul National University, 08826 Seoul, Republic of Korea
[e] School of Medicine, Department of Histology and Embryology, Marmara University, 34854 Istanbul, Turkey
[f] Esteworld Altunizade Plastic Surgery Complex, 34662 Istanbul, Turkey

ARTICLE INFO

Keywords:
Bilayered hydrogels
Osteochondral defect
Foreign body response
M1/M2 macrophage
Transcriptomic analysis

ABSTRACT

Addressing osteochondral defects, the objective of current study was to synthesize bilayered hydrogel, where the cartilage layer was formed by alginate (Alg)-polyacrylamide (PAAm) with and without the addition of TGF-β3 and bone layer by laponite XLS/Alg-PAAm and characterize by *in vitro* and *in vivo* experiments. Exceeding the mechanical strength of Alg-PAAm (32.95 ± 1.23 kPa) and XLS based (317.5 ± 21.72 kPa) hydrogels, XLS/Alg-PAAm hydrogel (469.7 ± 6.1 kPa) activated macrophages towards M2 phenotype and stimulated the expression of anti-inflammatory factors. The addition of TGF-β3 accelerated transition of macrophage polarization, especially between day 4 and 7. The expression levels of M1-related genes such as CD80, iNOS and TNF-α decreased gradually after day 4, reaching lowest values at day 13, whereas the expression levels of M2-related genes, CD206, Arg1 and STAT6 significantly increased promoting M2 macrophage polarization, which might be associated with accelerated bone repair. Moreover, bilayer structure exhibited a better cell viability as well as repairment thorough the XLS contents. *In vivo* histological examinations verified the significant surface regularity and hyaline like tissue formation employment, along with synchronized degradation profile of the hydrogel with tissue healing at the end of 12 weeks. A mechanically durable, biocompatible and immunocompatible hydrogel was formulated to be utilized in bone-cartilage engineering applications.

1. Introduction

Osteochondral tissue regeneration is a complex phenomenon due to the distinct composition of osteogenic and chondrogenic regions. The increasing rate of osteochondral defects due to trauma and injuries in aging population causes severe pain and economic burden to patients [1]. Although there are surgical treatments (*i.e.*, microfracture) along with cell therapies and grafting technologies, these procedures have not yet been fully recapitulating the structure and function of damaged regions. Furthermore, the surgical and cell therapies may end up with the undesired fibrocartilage formations [2] and potential immune reactions following the grafting procedures through autografts or allografts remain as a challenge in treatments. Therefore, it is essential to develop advanced biomaterials to serve as successful osteochondral tissue constructs harmonizing with the patients' body with respect to both cartilage and subchondral bone. Recently, biomaterials are becoming momentous in such biomedical applications despite their possible failures to reach beyond the limits of the laboratory due to the foreign body responses (FBR). Implantation induces an immune response characterized by the recruitment of proinflammatory macrophages to the tissue-biomaterial interface [3]. Therefore, FBR and related interactions between macrophages and host immune responses are essential for the selection of biomaterials. The rapid prototyping technologies, recently, enable the development of patient-specific hydrogel-based biomaterials, which resemble osteochondral tissues with respect to biological (*i.e.*, biocompatibility, biodegradation) and mechanical (*i.e.*, elastic and compression moduli) aspects, significant for such load bearing tissue applications [4,5]. Researchers have focused on better mimicking the interface of cartilage-bone tissues *via* multi-layered hydrogel structures representing the native structure. For instance, a bilayer hydrogel construct was developed for osteochondral regeneration where alginate (Alg) based upper hydrogel (chondral layer) was grafted onto acrylamide (AAm) based lower hydrogel (bone layer) by the two-step cross-linking [6]. Similarly, multiphasic osteochondral tissue constructs were fabricated *via* additive manufacturing technique by using nanocrystalline hydroxyapatite (nHA) particles for subchondral bone layers and chondrogenic growth factors for the cartilage layer [7]. The results indicated that nHA particles

* Corresponding author.
E-mail address: ozlem.yesil.celiktas@ege.edu.tr (O. Yesil-Celiktas).

http://dx.doi.org/10.1016/j.msec.2022.112721
Received 1 October 2021; Received in revised form 5 February 2022; Accepted 14 February 2022
Available online 19 February 2022

improved the mechanical properties of multiphasic constructs. Similar mechanical improvements of hydrogels have been reported with the laponite nanoclay [8] which has been shown to promote osteogenic differentiation of human mesenchymal stem cells in two-dimensional culture [9]. Notably, having an electrostatic interaction with polyacrylamide (PAAm) polymer causing self-healing of the gel [10], laponite nanoclay not only serves as an enhancer for mechanical strength of biocompatible polymers but also acts as a crosslinker for several hydrogel systems including PAAm [11].

The aim of the present study was to optimize the synthesis of a bilayered laponite XLS/Alg-PAAm composite hydrogel, investigate the immunocompatibility using a comprehensive *in vitro* 3D model and further test the efficacy in a preclinically relevant animal model of osteochondral defect in rats. We hypothesized that if the cartilage layer is formed with Alg-PAAm and bone layer with laponite XLS/Alg-PAAm, then the formulated hydrogel will be mechanically durable, biocompatible and immunocompatible. The method was optimized to achieve grafted chondrogenic and osteogenic layers of bilayer composite XLS/Alg-PAAm structure. The immune response was determined including release of proinflammatory and anti-inflammatory macrophages, cytokines, gene expression levels and cell proliferation towards the hydrogels. Furthermore, rat model was used to evaluate the repair of osteochondral defects *in vivo*.

2. Materials and methods

2.1. Synthesis of XLS/Alg-PAAm hydrogels

A three-step crosslinking procedure was applied for the synthesis of bilayer composite hydrogels. To prepare XLS based osteogenic layer (at bottom), a medium molecular weight alginate from brown algae (Sigma A2033, μ > 2000 cP, Mv = 900–1000 kDa, 1,4-linked β-D-mannuronic acid (M) and 1,4 α-L-guluronic acid (G) residues ratio (M/G block ratio) is 1.6) (A2033, Sigma-Aldrich) and acrylamide (AAm; A8887, Sigma-Aldrich) were dissolved at the ratio of 1:6 (*w*/w) in deionized (DI) water, and the total polymer concentrations were varied as 10%, 20% and 30% (w/w) in the solution. For the gelation process, laponite XLS (5% (w/w), BYK Additives Inc.), *N*,*N*,*N*′,*N*′-tetramethyl ethylenediamine (TEMED; T7024, Sigma-Aldrich), and ammonium persulfate (0.2 M, AP; A9164, Sigma-Aldrich) were used as crosslinker, accelerator and photo-initiator, respectively.

The chondrogenic layer (at top) was prepared with and without addition of TGF-β3 by using similar method described for osteogenic layer. Briefly, Alg-PAAm hydrogels with the total polymer concentrations of 10%, 20% and 30% (*w*/w) were prepared in DI water where the Alg and AAm ratio was kept as 1:6 (w/w). Different from the bottom layer formulation, *N*,*N*-methylenebis(acrylamide) (0.1 M, MBAA; M7279, Sigma-Aldrich) was used as crosslinker for covalently crosslinking of PAAm. For the TGF-β3 incorporated Alg-PAAm hydrogel production (Alg-PAAm$_{TGF\text{-}\beta3}$), TGF-β3 (15 ng per 0.55 g of hydrogel) was added into Alg-PAAm pre-solution simultaneously with the crosslinking agents.

To achieve the desired bilayered composite structures, the chondrogenic and osteogenic layer ratio was fixed as 1:4 in depth, the pre-solution of XLS-based hydrogel was poured into the bottom of cylindrical glass mold (2 mm in diameter and depth) and cured at + 4 °C for 24 h to form the osteogenic layer. Following, the pre-solutions of chondrogenic layer (Alg-PAAm and Alg-PAAm$_{TGF\text{-}\beta3}$) were prepared and poured into the partially filled glass mold to achieve chondrogenic layer at top and incubated at 50 °C for 3 h. In order to complete crosslinking *via* multivalent cations, resulted XLS/Alg-PAAm and TGF-β3 loaded XLS/Alg-PAAm$_{TGF\text{-}\beta3}$ hydrogel structures were immersed into calcium chloride (0.3 M) ($CaCl_2$; 102,382, Merck) for 1 h.

2.2. Characterization

The compressive stress-strain measurements of hydrogels were performed by using 50 N load cell Instron Model 3342 testing apparatus with 1 mm/min strain. The compression moduli were calculated due to the linear regions of stress-strain curves. For the analysis, hydrogels (20 mm in diameter and 4 mm in depth) were prepared, and all experiments were performed in triplicate.

The chemical cross-linking of the samples was characterized by a Fourier transform-infrared (FTIR) spectrometer (PerkinElmer Spectrum 100) between the wavelengths of 400–4000 cm^{-1}. Scanning Electron Microscope (SEM) was used to characterize morphology of hydrogel samples. The samples were mounted on a metal stub and coated with gold-palladium under vacuum at Leica EM ACE600 sputter-coater, and then the SEM images were taken by FEG SEM (Thermo Scientific, Apreo S, Netherlands).

The swelling behavior of hydrogels was examined in PBS (1 ×) solution at 37 °C. The initial weights (W_{int}) were obtained following the drying process of hydrogels (n = 3). They were re-immersed into PBS for 24 h and then reweighed after the excess water was removed from the swollen hydrogels (W_{wet}). The equilibrium swelling ratio was calculated with the Eq. (1) [12]:

$$\text{Swelling ratio } (\%) = (W_{wet} - W_{int})/W_{int} \times 100 \quad (1)$$

For the *in vitro* degradation test, the hydrogel samples were incubated in PBS (10 mL, pH 7.4) under 37 °C and constant agitation (75 rpm), and they were rinsed in DI water at pre-determined intervals. Following, samples were lyophilized, and dry weights were measured. The degradation was expressed by using Eq. (2) where the W_0 and W_d are the weights before and after the incubation, respectively.

$$\textit{Degradation } (\%) = (W_0 - W_d)/W_0 \times 100 \quad (2)$$

2.3. In vitro biocompatibility

A differentiated chondrogenic cell line from mouse teratocarcinoma cells (ATDC5), and human fetal osteoblastic cells (HFOB 1.19) were obtained from American Cell Culture Collection (ATCC, Mannassas, VA, USA). Cells were maintained in Dulbecco's Modified Eagle Medium (DMEM) and Ham's F12 medium at a ratio of 1:1 (DMEM F12) containing 10% (*v*/v) Fetal Bovine Serum (FBS), 1% (v/v) L-glutamine (200 mM), 0.1% (v/v) gentamicin (10 mg/mL) and 1% (v/v) penicillin/streptomycin (10.000 U-10 mg/mL) in 75-cm^2 cell culture flasks to grow to confluency (≈90%) at humidified incubator (5% CO_2, 37 °C), received fresh medium every 2 days and subcultured every 5–7 days. All cell culture reagents were supplied by Sigma-Aldrich.

According to *ISO 10993-12*: *Sample preparation and reference materials* standards [13], the 10% (*w*/w), 20% (w/w) and 30% (w/w) Alg-PAAm, XLS based and XLS/Alg-PAAm hydrogels were produced in equal sizes (4 mm in diameter and depth) using suitable molds. After DI water-PBS (1 ×) washing and following UV sterilization, hydrogels were transferred into sterile falcons at the recommended ratio of surface area/extraction volume (3 cm^2/mL) and incubated at 37 °C for 72 h with the addition of growth media (DMEM F12 containing 0.1% gentamicin and 1% sodium bicarbonate).

In accordance with *ISO 10993-5*: *Tests for in vitro cytotoxicity standards* [14], 10%, 20% and 30% (*w*/w) Alg-PAAm, XLS based and XLS/Alg-PAAm hydrogel extracts were tested on ATDC5 and HFOB cells using 3-(4,5-dimethylthiazol-2-yl)-2,5-diphenyl tetrazolium bromide (MTT) assay. Cells were seeded in 96-well plates (1 × 10^4 cells/well) and incubated overnight at 37 °C and 5% CO_2. Thereafter, the medium was removed and certain ratios (1/1, 1/2, 1/4, 1/8, 1/16 in growth medium) of hydrogel extracts (100 μL) were added to each well as test groups. Untreated cells in growth medium and the cells kept in dimethyl sulfoxide (DMSO, Sigma-Aldrich) were considered as the positive and negative controls, respectively. After 72 h of incubation, cell supernatant was removed, 10% MTT solution (diluted in growth medium from 5 mg/mL stock solution, M5655, Sigma-Aldrich) was added to each well (100 μL) and incubated for 3 h at 37 °C. Then, MTT was removed and DMSO was added to each well at 100 μL, subsequently the absorbance was measured by a microplate

reader at 570 nm (BioTek, Korea). Cell viability (%) was calculated with GraphPad Prism 7.0 program [15].

2.4. Immune response induced by bilayered XLS/Alg-PAAm hydrogels

In vitro 3D gelatin methacryloyl (GelMA)-methacrylated hyaluronic acid (-MeHA) model for the assessment of immune response induced by hydrogels was validated *via* following steps. First, XLS/Alg-PAAm and XLS/Alg-PAAm$_{TGF-\beta3}$ hydrogels were transferred to 48-well cell culture plates. GelMA-MeHA prepolymer solution was prepared in the dark at 70 °C by dissolving GelMA (5% (*w/v*)) and MeHA (0.1% (w/v)) in DMEM F12 medium containing photoinitiator 2-Hydroxy-4′-(2-hydroxyethoxy)-2-methylpropiophenone (0.5% (w/v), Irgacure 2959). Following, the trypsinized cultures of ATDC5, mouse connective tissue fibroblast cells (L929, ATCC, Manassas, VA, USA), mouse macrophage cells (Raw 264.7, ATCC, Manassas, VA, USA) and HFOB cells were resuspended in 37 °C GelMA-MeHA prepolymer solution (3.25×10^5 cell/mL) and the cell-prepolymer mixture was transferred per well to completely cover the hydrogel previously placed and photocrosslinked using UV light (Omnicure S2000, Lumen Dynamics, Canada) at 800 mW/cm^2 for 30 s with 8 cm distance to form *in vitro* 3D GelMA-MeHA model. 3D model was incubated at 37 °C and 5% CO_2 for 13 days and cell culture medium (LPS-free or with 1 μg/mL LPS) has been changed every two days. At predetermined time points (days 1, 4, 7, 10 and 13), *in vitro* 3D GelMA-MeHA models were used to assess the viability, location and immune response of the cells.

2.4.1. Assessment of cell viability and cytotoxicity

The effect of XLS/Alg-PAAm hydrogels on cell viability was assessed at predetermined time points using Cell Counting Kit 8 (CCK-8) (ab228554, Abcam) quantitatively and LIVE/DEAD™ viability/cytotoxicity assay kit (L3224, Molecular Probes, Invitrogen) qualitatively. Briefly, the medium on the 3D GelMA-MeHA model was removed, followed by addition of CCK-8 solution (10:1 ratio of growth medium: CCK-8 reagent) to each well and incubation for 3 h at 37 °C. Then, the absorbance was measured using a microplate reader (BioTek, Korea) at 450 nm. For Live&Dead assay, 3D GelMA-MeHA model was washed with PBS (1 ×) and stained with calcein acetoxymethyl ester (2 μM) and ethidium homodimer-1 (4 μM) for 90 min at 37 °C and observed by fluorescence microscopy (Zeiss, Axio Vert.A1).

2.4.2. Tracking of cell proliferation and location

To evaluate the cell proliferation, resuspended L929, Raw 264.7, HFOB and ATDC5 cells were stained prior to mixing with prepolymer solution with Red CellTracker™ CMTPX (15 μM, C34552 Thermo Fisher Scientific), Green CellTracker™ CMFDA (25 μM, C7025, Thermo Fisher Scientific), Hoechst 33258 (15 μM, B2883, Sigma-Aldrich) for 45 min and Acrydine Orange (25 μM, A6014 Sigma-Aldrich) for 25 min at 37 °C and 5% CO_2. The labeled cells were imaged by fluorescence microscopy (Zeiss, Axio Vert.A1) at predetermined time points.

2.4.3. Analyses of cytokines

For proinflammatory and anti-inflammatory cytokine analyses, the supernatants were collected at predetermined time points. The IL-6 and IL-10 concentrations in the supernatants were quantified as triplicates using Mouse IL-6 and IL-10 ELISA Kits (Legend Max™, Biolegend) according to the manufacturer's instructions.

2.4.4. Assessment of macrophage polarization

For the assessment of M1 and M2 macrophage phenotypes, immunocytochemical (ICC) and qRT-PCR analyses were performed at predetermined time points. Cells were harvested individually from the 3D model using collagenase solution (100 U/mL, 17018-029 Gibco) prepared in PBS (1 ×) 1 h at 37 °C. For ICC analyses, collected cells were seeded in a 48-well plate and incubated overnight. Following, cells ells were fixed by paraformaldehyde (4% (*w/v*)) for 30 min at 4 °C and permeabilized with Triton X-100 (0.1% (*v*/v)) for 15 min at room temperature (RT). For blocking, cells were incubated in bovine serum albumin (1% (w/v), BSA, GoldBio A-420-100) solution in PBS (1 ×) at RT for 1 h and incubated overnight at 4 °C with Armenian hamster monoclonal to CD80 (1:80 dilution, ab106162, Abcam) and Mouse monoclonal to mannose receptor CD206 (1:100 dilution, ab8918, Abcam) primary antibodies (M1 and M2 markers, respectively) in Tris-Buffered Saline solution containing Triton X-100 (0.025% *v*/v) and BSA (3% *w/v*). On the following day, the cells were washed with PBS (1 ×) and incubated with Alexa Fluor 488-Goat Anti-Armenian hamster (1:200 dilution, ab173003, Abcam) and Alexa Fluor 594-Goat Anti-Mouse (1:200 dilution, ab150116, Abcam) secondary antibodies (for CD80 and CD206, respectively) for 1 h at RT. Subsequently, DAPI staining (1.5 μg/μL, D9542, Sigma-Aldrich) was performed for 15 min and cells were photographed using microscope (Zeiss, Axio Vert.A1). NIH ImageJ software was used to quantify CD80 and CD206 and the M1/M2 expression ratio was calculated. For qRT-PCR analyses, total RNA was isolated from collected cells cultured in 3D model at predetermined time points, by using RNeasy Plus Mini Kit (Qiagen, Germany) and then cDNA was synthesized from equal amounts of RNA for each group with RT2 First Strand Kit (Qiagen, Germany) for each group. Gene expression profiles of CD80, CD68, iNOS, TNF-alpha (as M1 polarization), CD206, Arg1, STAT6 (as M2 polarization) genes (Table S1) were determined by qRT-PCR method using RT^2 SYBR Green qPCR Mastermix *via* LightCycler 480 Instrument II (Roche, Germany). The gene expression levels of each gene was normalized using *HPRT1*, *GAPDH* and *ACTB* housekeeping genes and fold regulation data was calculated using the 2-ΔΔCt method. Data were shown by dividing the normalized gene expression in each day sample (Day 4, 7, 10, 13) by the normalized gene expression in day 1 sample for all hydrogel groups.

2.5. In vivo osteochondral defect model

2.5.1. Animals

All animal procedures were approved by the Committee of Marmara University Animal Care and Use (approval number 69.2019.mar). Eighteen healthy male Sprague Dawley rats at 12-weeks-old (and weighing 300–350 g) were used for the study. They were housed in a light and temperature-controlled room. Food and water were given *ad libitum*. To evaluate *in vivo* effectiveness of designed XLS/Alg-PAAm hydrogels, animals were randomly divided into three groups and filled with XLS/Alg-PAAm$_{TGF-\beta3}$ ($n = 6$), XLS/Alg-PAAm hydrogel (n = 6) or left untreated as control.

2.5.2. Surgical procedure for the generation of osteochondral defect model

The rats were anesthetized with ketamine (50 mg/kg, Ketalar 2%; Pfizer) and xylazine (10 mg/kg, Alfazyne 2%, Alfasan) administered by intraperitoneal injection. A parapatellar skin incision was made on the medial side of knee joints to expose the articular surface. Following the incision synovial capsule, the patella was dislocated to expose trochlear groove. Subsequently, a cylindrical osteochondral defect (1.5 mm in diameter and 3.0 mm in depth) was generated in the center of trochlea using a dental drill with the knee flexed [16]. All debris was removed and irrigated with saline. Then, the created defect was filled with XLS/Alg-PAAm$_{TGF-\beta3}$, XLS/Alg-PAAm hydrogel, or left untreated as control. After relocation of the patella, the joint capsule and subcutaneous tissue were carefully closed. At 12 weeks, all rats were sacrificed, and knees were harvested.

2.5.3. Histological examinations

For light microscopic investigations, samples from rats were excised and fixed in 10% neutral buffered formalin. Demineralization of the tissues was performed with EDTA (Sigma-Aldrich) at RT. Samples were then washed in PBS (1 ×) and dehydrated in ascending series of ethanol, cleared with xylene and embedded in paraffin. Tissue sections (5 μm) were cut on a rotary microtome (Leica RM2155, Germany), mounted on a microscope glass and stained with hematoxylin and eosin (H&E), Safranin O/Fast Green, Masson's trichrome, Toluidine blue (TB) and PAS stains for morphological evaluation of the cartilage and bone tissue repair. Sections were examined by a histologist being blinded to experimental groups based on a modified scoring system for osteochondral tissue repair thorough

cartilage and subchondral bone assessment [17,18]. The cartilage repair in osteochondral defects of rats were scored regarding to morphology of new surface tissue and new cartilage tissue, thickness of new cartilage, joint surface regularity, chondrocyte distribution, cellularity and Safranin O staining. On the slides stained by Masson's trichrome, the new bone formation was scored semi quantitatively as 0: No bone formation, 1: Little amount of bone formation, 2: Moderate amount of bone formation, 3: Large amount of bone formation, 4: Near normal appearance. Finally, sections were photographed under an Olympus DP72 CCD camera attached BX51 photomicroscope (Olympus, Tokyo, Japan).

2.6. Statistical analysis

Statistical analyses were carried out by *One-way variance analysis* (*one-direction ANOVA*, *Tukey's Multiple Comparison Test*) *via* Prism 8.3 (GraphPad, San Diego, CA, USA) with ±95% confidence interval and p values<0.05 were considered statistically significant.

3. Results and discussion

3.1. Synthesis of XLS/Alg-PAAm hydrogels, characterization and in vitro biocompatibility

Having proven biocompatibility as implantable cartilage material with and without growth factor loaded nanoparticles [19], Alg-PAAm hydrogels were used to generate a more complex and graded osteochondral tissue structure with the addition of laponite XLS nanoclay. A series of compression tests were performed to investigate the mechanical properties of bilayer XLS/Alg-PAAm hydrogel in response to the ratio of its parents. As the ideal replacement of osteochondral layer must provide the certain mechanical strength supporting the new tissue formation [20], the initial attempt was to optimize total polymer (Alg + PAAm) concentrations (10%, 20% and 30% (*w*/w)) for both chondrogenic and osteogenic layers due to the mechanical and biocompatible properties. As for the compression results, hydrogels consisting of 20% (*w*/w) and 30% (w/w) total polymer revealed similar modulus values ($p > 0.05$; 51.77 ± 3.99 kPa and 57.15 ± 1.22 kPa, respectively) which were 1.6- and 1.7- times higher than that of 10% (*w*/w) total polymer, respectively (Fig. 1A). Although the higher total polymer concentrations showed higher mechanical strength, the highest cell viability of both ATDC5 (>90%) (Fig. 1B) and HFOB (>80%) (Fig. S1) were observed with 10% (*w*/w) total polymer extracts, and it was considered as an opportunity to expedite healing and maintain chondrocytes survived within the neighbor tissues as the cartilage exhibits poor self-healing capacity due to the lack of vascularization [21]. Besides, the degradation profile of 10% (*w*/w) total polymer due to the slight cleavage of polymer chains was appropriate as the initial healing of cartilage defects occurs in 1–3 months [22]. Hence, Alg-PAAm hydrogel including 10% (*w*/w) total polymer was selected for chondrogenic layer replacement.

As for the load-bearing osteogenic layer formulation, the mechanical strength and revascularization synchronizing with new bone ingrowth were

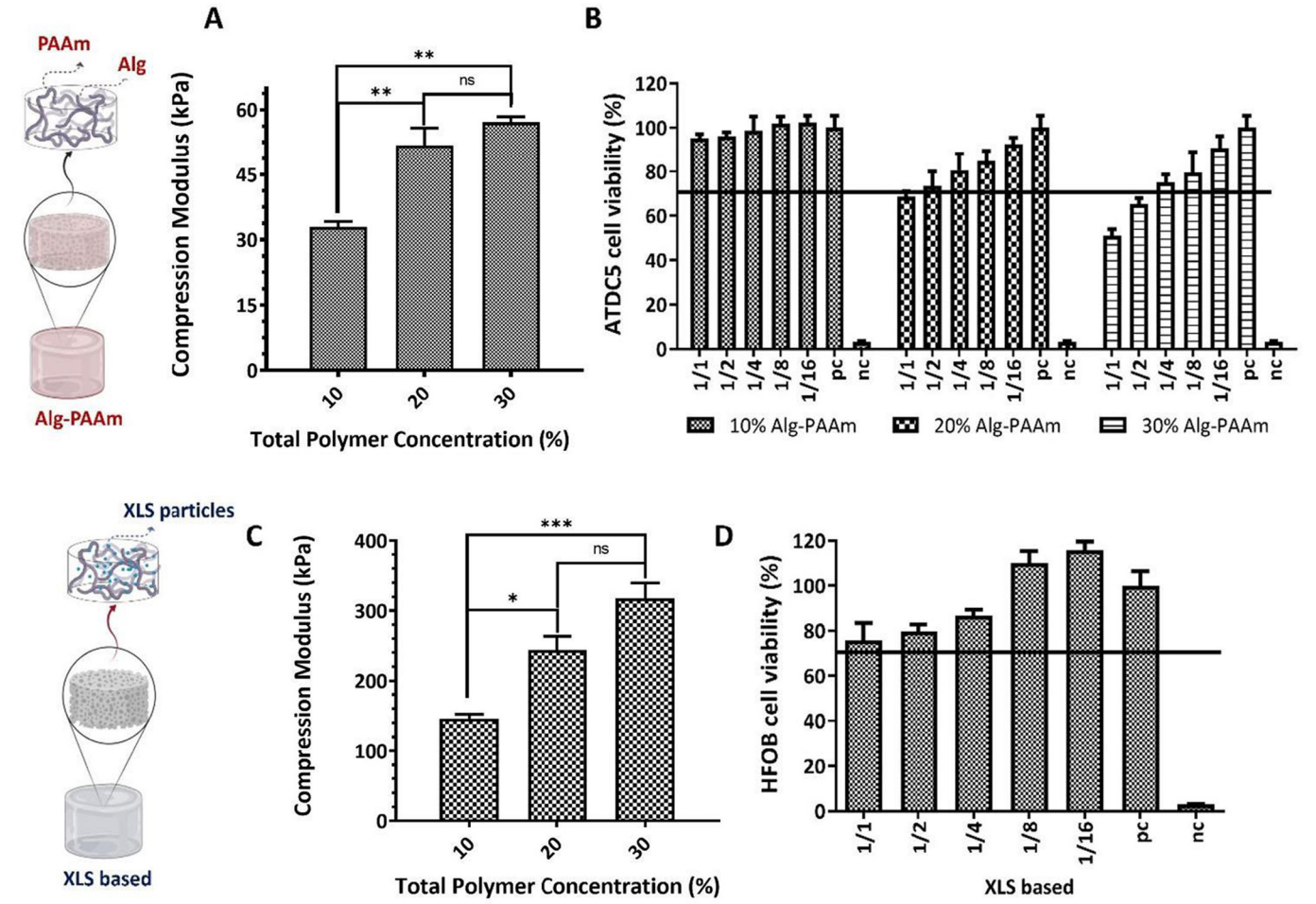

Fig. 1. Schematics depicting the hydrogel structures, and characterizations of individual hydrogels. (A) Average compression test results of Alg-PAAm hydrogels with 10%, 20% and 30% total polymer concentration ($n = 3$). (B) The cell viability of ATDC5 cells in the hydrogel extracts at 72 h. (Schematics of hydrogels were created with BioRender.com) (C) Compression moduli of %5 (*w*/w) XLS included Alg-PAAm hydrogel formulations (n = 3). (D) Displayed cell viability levels of HFOB cells within the different extract concentrations of XLS based hydrogels (%5 (w/w) XLS included Alg-PAAm hydrogels with 30% total polymer concentration) at 72 h. pc: positive control, nc: negative control. ns: $p > 0.05$, $^{*}p < 0.05$, $^{**}p < 0.01$, $^{***}p < 0.001$; One-Way ANOVA, Tukey's Multiple Comparison Test.

essential. Therefore, 5% (w/w) XLS concentrations holding a great promise for treating bone defects were added to Alg-PAAm hydrogel formulations.

Laponite (*i.e.*, XLS), as a smectite mineral family member, is one of the most commonly used biocompatible clay minerals in various biomedical applications to promote cell proliferation, differentiation and adhesion [9]. Accelerating the gelation process through hydrogen bonds with Alg matrices [23], XLS nanoplatelets were able to endow Alg-PAAm hydrogels with superior mechanical properties. As such, with the addition of 5% (*w*/w) XLS to Alg-PAAm hydrogels containing 10%, 20% and 30% (w/w) total polymers, 4.4, 4.7- and 5.6-times higher compression modulus values were obtained, respectively (Fig. 1C), and Alg-PAAm hydrogels with 5% (*w*/w) XLS and 30% (w/w) total polymer were selected for the osteogenic layer. Compared with our previous data on the mechanical strength of polymer-based nanoparticle added Alg-PAAm hydrogel (59.79 ± 1.58 kPa) [19], the superior effect of XLS addition was proven with 10% (*w*/w) Alg-PAAm hydrogels (145.49 ± 6.54 kPa). Moreover, cell viability for HFOB cells were observed to be promoted by the addition of 5% (w/w) XLS into Alg-PAAm structure with 30% (w/w) total polymer (Fig. 1D) without any growth factor supplementation. Similar to our study, laponite/Alg nanocomposite extracts were shown to demonstrate better cell proliferation for osteoblast-like cells compared to Alg extract and growth medium alone, due to the release of silica, upregulating the expression of genes involved in osteoblast proliferation and differentiation [24]. Considering, the *in vitro/in vivo* studies where laponite-added hydrogels were used as tissue scaffolds, the anionic charges on the surface of laponite particles and their activities at the molecular and genetic level were shown to induce cell attachment, proliferation, differentiation and new formation in the surrounding tissues [25]. Following the individual hydrogels, the mechanical behavior of bilayer structure was assessed through the stress-strain curves obtained during the compression analysis (Fig. 2A). XLS/Alg-PAAm hydrogels resulted in an average compressive modulus of 469.7 ± 6.1 kPa, which was exceeded the sum of the modulus of its parents, Alg-PAAm (32.95 ± 1.23 kPa) and XLS based (317.5 ± 21.72 kPa) hydrogels. The affinity and penetration between two layers were confirmed as the interface remained stable during compression [26].

The formation of bilayer structure and characteristic functional groups of XLS/Alg-PAAm hydrogels were also identified with FTIR measurements (Fig. 2B). One of the common characteristic band between 3200 and 3500 cm^{-1} was found to be associated with O − H stretching peak [27] supporting the interpenetrating network formation of Alg-PAAm hydrogels [28]. The other dominant band around 1600 cm^{-1} was correspond to the stretching carbonyl groups (–C = O) of PAAm where the band around 1020 cm^{-1} were due to the SiO stretching of XLS clay [29]. Furthermore, compared to FTIR spectrum of Alg-PAAm, increased intensity of Si-O-Si stretching was observed in both XLS based and XLS/Alg-PAAm hydrogels, attributing to the interactions between Alg-PAAm polymer network and XLS clay through Si-OH groups [12]. Notably, activity of XLS nanoplatelets as physical crosslinker was strongly confirmed with these results. Consistent with the FTIR results, SEM images showed the two penetrated layers of XLS/Alg-PAAm hydrogels (Fig. 2C) as well as the interface formation between layers. Although Alg-PAAm hydrogels exhibited very smooth and compact nature, XLS based hydrogels showed porous surface where the pore diameter varied from 139.6 nm to 837.5 nm, confirming the distribution of XLS within the hydrogel structure. The swelling behaviors of individual hydrogels as well as their degradations were measured to estimate the synchronization between hydrogels deformations and tissue healing. Consistency between swelling (Fig. 2D) and degradation (Fig. 2E) rates revealed that the physical degradation was strongly related to the presence of XLS. As such, comparing the Alg-PAAm and XLS based hydrogels, it was obvious that the XLS based hydrogel lost its structural integrity faster than Alg-PAAm hydrogels and swelled about 2 times higher than Alg-PAAm at the end of first week. Similar pattern was observed with the degradation tests. The weight loss of Alg-PAAm hydrogels within the first week was 7.19% whereas, 24.35% and 35.36% for both XLS based and XLS/Alg-PAAm hydrogels, respectively. Although the rate of weight loss decreased to 10–15% in both hydrogel and became stable at the following weeks, their degradation rates were still higher than that of Alg-PAAm of which total degradation was 45.85% even at the 12th weeks. In addition, the cell viability results of ATDC5 and HFOB cells in the extract of XLS/Alg-PAAm hydrogels have shown the biocompatibility for both chondrogenic and osteoblastic cells, with cell viabilities above 70% (Fig. 2F). Therefore, it is concluded that the bilayered composite hydrogel can be safely utilized for bone-cartilage interface in tissue engineering applications.

3.2. Immune response induced by XLS/Alg-PAAm hydrogels

Reducing the function of biomaterial and causing subsequent life-threatening reactions within the body, immune response may lead to implant failure. Hence, to increase the reliability and function of implantable biomaterials, it is imperative to understand the long-term immune response [30]. A straight-chain anionic, hydrophilic and colloidal polyuronic acid structural polysaccharide capable of gelation was used in the preparation of bilayer composite hydrogels as the main component, in our study. Alg hydrogels, formed through physical crosslinking, provided highly tunable properties. Thanks to its versatile and biological properties such as biocompatibility, non-immunogenicity (low-immunological response), hydrophilicity, pH-sensitivity, bioadhesion, chelating ability, water solubility, and high absorption capacity, Alg is widely used in biomedical applications as in protein/drug delivery systems, tissue regeneration, and wound healing [15,31]. Herein, the immune response against XLS/Alg-PAAm hydrogels was determined prior to *in vivo* examination through a 3D *in vitro* bioengineered model (Fig. 3A) mimicking the complexity of *in vivo* inflammatory state. During the development of rheumatoid arthritis and osteoarthritis, which are associated with osteochondral defects, macrophages mainly polarize towards M1 phenotype and release proinflammatory cytokines. High release of cytokines such as IL-6, TNF-α and IL-18 causes a sustained inflammatory response in tissues and promotes bone and cartilage damage [32]. As LPS is an important pro-inflammatory inducer [33], the current study used LPS, which provides a sustained inflammatory environment, to continuously induce inflammation and establish a cell-based inflammation model. Within the joint, LPS stimulates pro-inflammatory macrophages through TLR4, resulting in the activation of a cascade of signaling events that lead to the production of inflammatory mediators [34].

The potential cytotoxicity of XLS/Alg-PAAm hydrogel was examined by CCK-8 and Live&Dead cell viability assays on L929, Raw264.7, HFOB and ATDC5 cells cultured in the 3D bioengineered model (Fig. 3B, C). According to CCK-8 assay results, cell viabilities were quantitatively increased day by day, mostly between day 4 and 7 ($p < 0.0001$). The Live&Dead assay results also showed that the cells adapted to LPS-free microenvironment in terms of promoted cell viability, proliferation and morphology. The cell distribution was observed to be homogeneous and the number of dead cells was lower than that of living cells even at the end of day 13. In contrast to LPS-free microenvironment, cell proliferation and morphology was found less supported in the presence of LPS. In addition, reduced adherence and poorly defined outlines of the cells were observed. The endotoxic nature of LPS thought to induce the oxidative stress in cultured cells during the prolonged cultivation and concomitantly higher number of dead cells in the LPS + compared to LPS- microenvironment [35,36]. These results showed that XLS/Alg-PAAm hydrogel had no cytotoxic effect for cells and did not affect cell viability.

Proliferation of L929, Raw264.7, HFOB and ATDC5 cells towards XLS/Alg-PAAm hydrogel was qualitatively examined by cell tracker fluorescence staining (Fig. 3D). The presence of LPS stimulated the proinflammatory state leading to increased proliferation of macrophages, as expected and adversely affected the proliferation of chondrocyte and osteoblast cells [37]. Migration of macrophages towards XLS/Alg-PAAm hydrogel by increasing their phagocytic abilities, enabled the removal of cell debris and minimized the foreign body response [38] towards XLS/Alg-PAAm hydrogel. Promoted macrophage proliferation in the presence of LPS proved the formation of desired proinflammatory environment. Moreover, increased number of L929 fibroblasts and the level of IL-10 along with the decreased IL-6 levels were observed during 13-day period in the LPS-microenvironment. These results were associated with the secretion of anti-inflammatory cytokines such as IL-10 during the healing process by

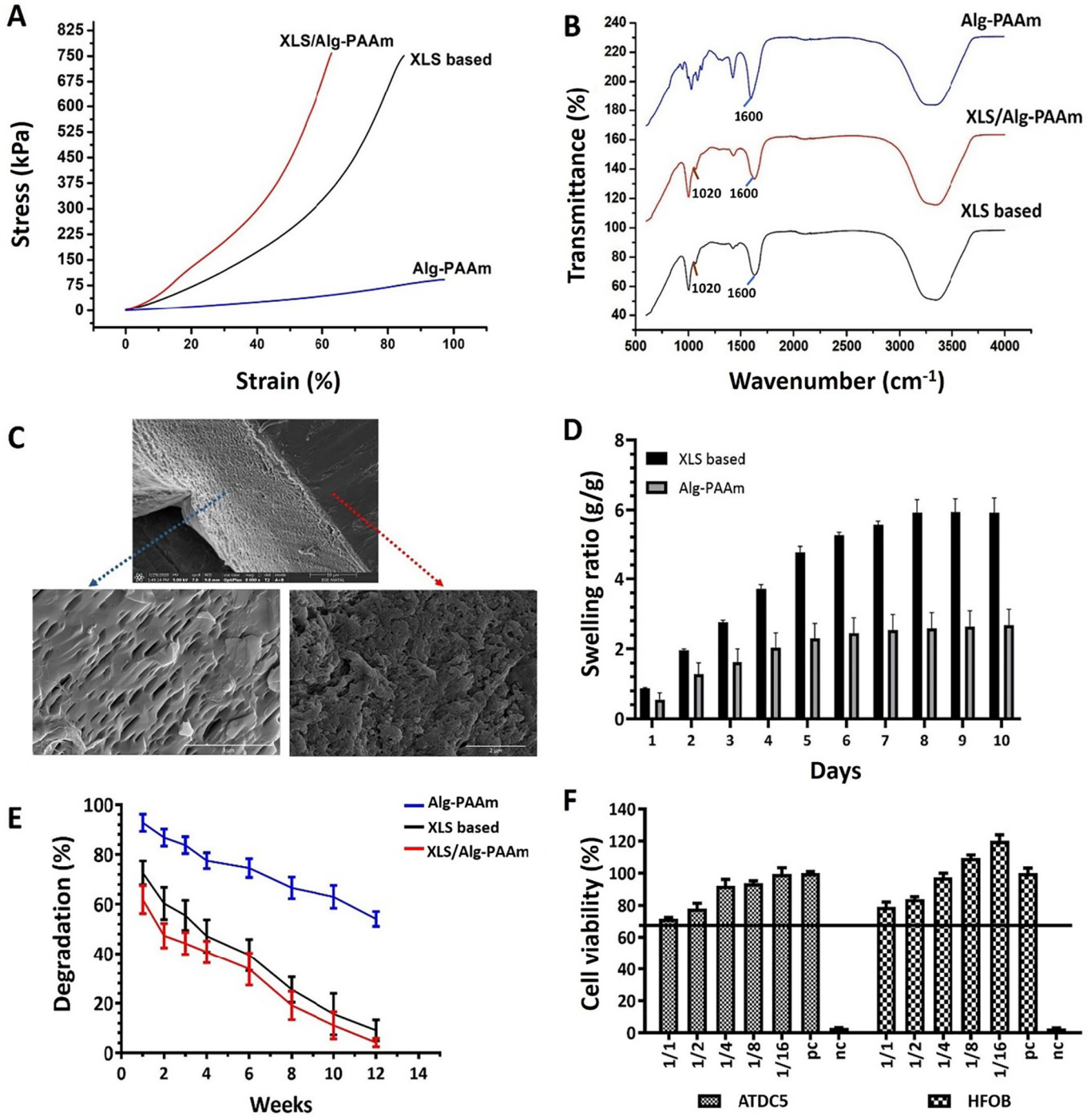

Fig. 2. Characterization of XLS/Alg-PAAm bilayer hydrogel structure. (A) Representative stress-strain curves and (B) FTIR spectra of Alg-PAAm, XLS based and XLS/Alg-PAAm hydrogels. (C) SEM micrographs of XLS/Alg-PAAm hydrogels composed of XLS based (left) and Alg-PAAm (right) hydrogels. (D) Swelling ratio and (E) Degradation rate of hydrogels. (F) The cell viability results of ATDC5 and HFOB cells in the XLS/Alg-PAAm hydrogel extracts at 72 h. pc: positive control, nc: negative control.

the macrophages, thereby promoting the proliferation of fibroblasts, collagen synthesis, and thus tissue healing [39]. The concentrations of IL-6 and IL-10 cytokines released from XLS/Alg-PAAm hydrogels within the generated 3D model were determined *via* ELISA analysis. In this study, the role of biomaterial-mediated modulation of macrophage polarization in the repair of cartilage-bone tissues with relatively poor regenerative capacities was sought to be discussed. The immune response is vital for efficient tissue repair and halting disease progression by controlling the proinflammatory environment associated with cartilage-bone damage [40]. Results revealed that in the LPS-free 3D model, macrophages stimulated the inflammatory response through the secreted IL-6 proinflammatory cytokines from day 1 (8.3 pg/mL) to day 4 (16.4 pg/mL) and initiated the cascade required to enter the recovery phase [41]. As the inflammatory phase begins immediately after the wound formation and generally lasts for 3–5 days [42], it was important to nominate the time points indicating the switch from destructive to constructive inflammatory state [43]. Hence, in accordance with the literature, the decreased concentration of IL-6 (5.8 pg/mL on day 13) ($p < 0.0001$) along with increasing IL-10 concentration from day 4 to day 13 (73.0 to 107.2 pg/mL) ($p < 0.0001$) (Fig. 4A, B) implicated the initiation of healing process as of day 4 [44]. Anti-inflammatory IL-10 suppresses proinflammatory cytokine production by activated M1 macrophages, limits cartilage damage and inhibits bone resorption, which is an

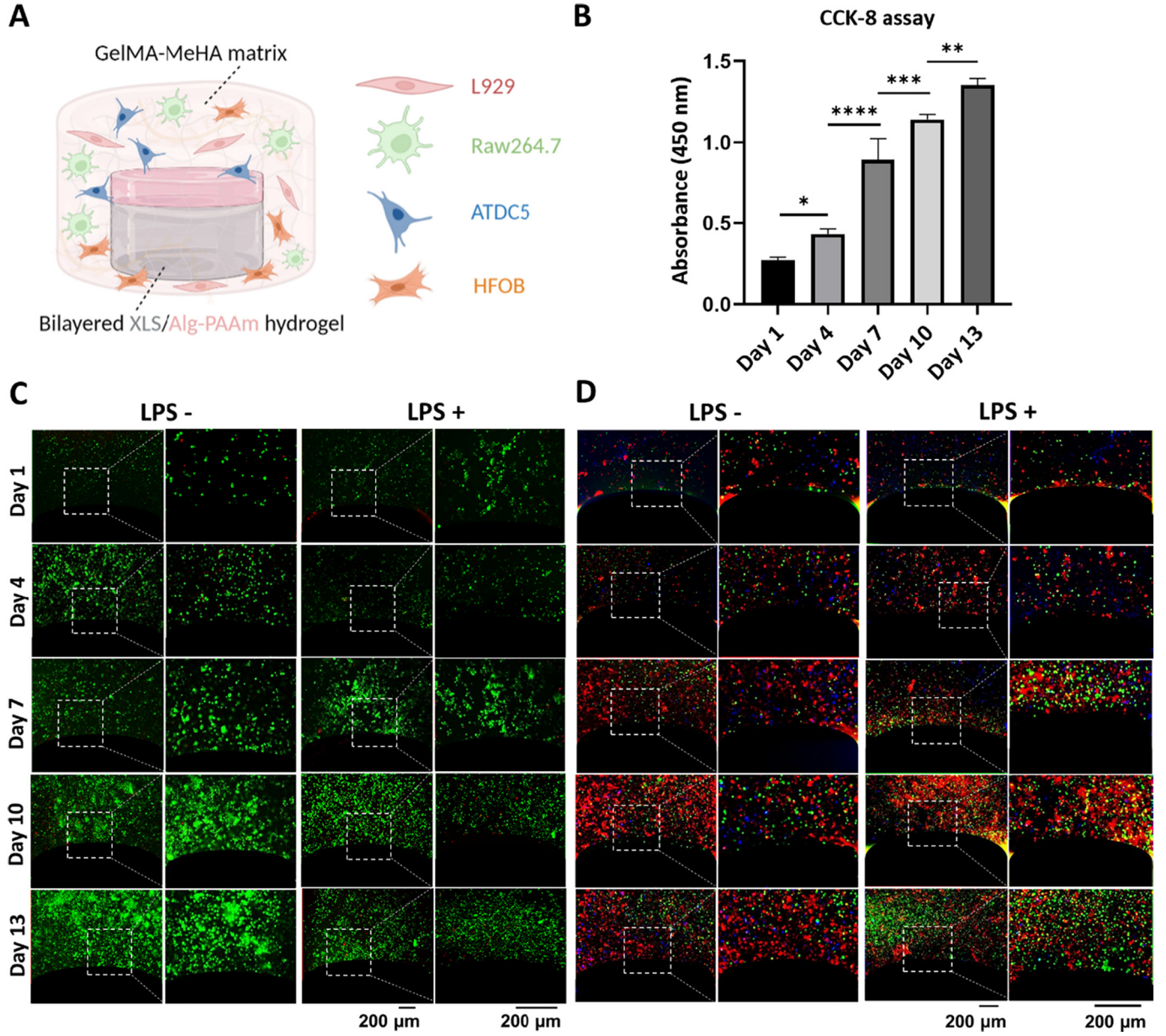

Fig. 3. Assessment of cell viability and proliferation. (A) Schematics depicting XLS/Alg-PAAm hydrogel-based 3D bioengineered model. (B) CCK-8 cell viability assay of L929, Raw264.7, HFOB and ATDC5 cells in the 3D model and quantification of the absorbances for 13 days. *$p < 0.05$, **$p < 0.01$, ***$p < 0.001$, ****$p < 0.0001$; One-Way ANOVA, Tukey's Multiple Comparison Test. (C) Cell viability after Live&Dead analysis of 3D model containing XLS/Alg-PAAm hydrogels where green fluorescent highlights live and red highlights dead cells, respectively. (D) CellTracker fluorescent staining to track the positions of cells in the 3D model against XLS/Alg-PAAm hydrogels. L929 red, Raw264.7 green, HFOB orange and ATDC5 blue. (Scale bar: 10× and 20×, Zeiss Axio Vert.A1).

important factor for osteoclast differentiation [45]. Xie et al. showed that inhibition of IL-6 inflammatory cytokines *via* IL-10 is a potent method to reduce inflammation and inhibit osteoclastogenesis [46]. Depending on the healing process, an increase in the level of predominant anti-inflammatory cytokine IL-10 is observed during the follow-up period [47] and various biomaterials were proven to increase IL-10 levels inducing osteogenesis by macrophage polarization to M2 macrophages [48]. *In vivo* studies to date show that regulating the behavior of macrophages through attenuation of the inflammatory environment in the joints and immunomodulation of biomaterials prevents joint destruction and promotes osteochondral defect regeneration [49].

As for LPS induced model, the inflammatory response was mediated by activated M1 macrophages [50] and an increase ($p < 0.0001$) in IL-6 concentration was observed during 13 days period, whereas IL-10 concentration decreased ($p < 0.0001$) as a result of excessive inflammatory response at the implant side. Addition of TGF-β3 as a trigger for the polarization of inflammatory M1 macrophages into reparative M2 macrophages [43] resulted with the maximum ($p < 0.0001$) IL-6 levels (159 pg/mL) reached during the first 24 h. Subsequently, IL-6 level decreased ($p < 0.0001$) to 70.6 pg/mL while IL-10 levels (32.4, 109.1, 150, 128.9, 152.2 pg/mL) increased ($p < 0.0001$) during the following 13 days. It was reported in our previous study [19], where *in vitro* TGF-β3 release from Alg-PAAm$_{TGF\text{-}\beta3}$ was observed with an initial burst release and reached 23% of total TGF-β3 on day 3. The protein adsorption tendency and hydrophobic interactions of hydrogel have been postulated to affect the release rate of TGF-β3 and resulted in a prolonged release of TGF-β3. Herein, the subsequent decrease of IL-6 and simultaneous increase of IL-10 levels during the following 13 days could be attributed to the prolonged release of TGF-β3 from XLS-PAAm-Alg $_{TGF\text{-}\beta3}$, with a cumulative release rate of approximately 45% up to day 13. Compared with the XLS/Alg-PAAm results

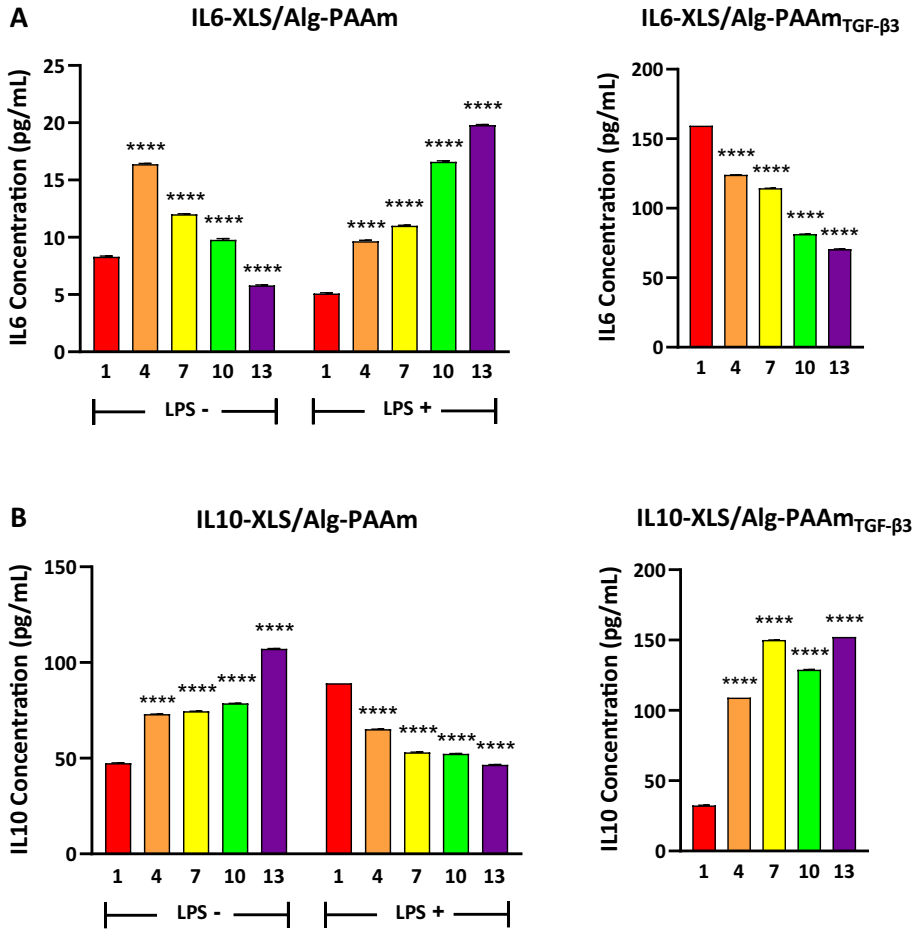

Fig. 4. Cytokine concentrations in the supernatant of the 3D model containing the XLS/Alg-PAAm hydrogel during 13 days. (A) Effects of healthy/inflammatory conditions and loading TGF-β3 into gel on IL-6 cytokine concentration against XLS/Alg-PAAm. (B) Effects of healthy/inflammatory conditions and loading TGF-β3 into gel on IL-10 cytokine concentration against XLS/Alg-PAAm. ****$p < 0.0001$; One-Way/Two-way ANOVA Tukey's Multiple Comparison Test performed to determine statistically significant differences in cytokine production ($n = 3$ independent experiments). Error bars represent standard deviation.

under both healthy (LPS-) and inflammatory (LPS +) conditions, the increases in cytokine concentrations were higher for XLS/Alg-PAAm$_{TGF-β3}$ (approximately 19 and 32-fold higher on day 1; 12 and 3.5-fold higher on day 13, respectively). Transforming growth factor β (TGF-β), one of the main immune and inflammatory factors responsible for cell proliferation, differentiation, angiogenesis, and regulation of immune responses, is known to be required for the induction and maintenance of chondrocyte and osteoblast phenotypes [51]. For that reason, various studies on the sustained release of TGF-β *via* microspheres and hydrogels have sought to increase particular chondrocyte proliferation and cartilage matrix deposition [52]. TGF-β is a highly pleiotropic cytokine that exists in three isoforms (TGF-β1, TGF-β2, and TGF-β3), synthesized by almost all cells and can signal to almost all cells and act in wide-range [53]. Besides its high anti-inflammatory effect, TGF-β3 is involved in regulating the interleukin network, IL-1 and IL-6 in particular [54]. From this point on, the duration and concentration of treatment are decisive for its pro-inflammatory or anti-inflammatory effects.

Sharkey et al. reported that TGF-β3 stimulated IL-6 production in a dose-dependent manner, with 50 ng/mL TGF-β3 causing a 13-fold increase after 24 h compared to the untreated control as well as other TGF-β isoforms [55]. High IL-6 proinflammatory response level in the first days of the early scar-free healing process induced by TGF-β3 should not be considered as a negative aspect since it may be associated with chondrocyte cell proliferation and differentiation in 3D culture as well as the immune response against the hydrogel [56]. The sequential activation of the M1 and M2 phenotypes of macrophages affects not only the initiation and regression of inflammation, but also the quality of tissue regeneration and remodeling [57]. Notably, macrophage polarization towards a more stable M1/M2 macrophage ratio or predominantly M2 phenotype [48] indicates the suitability of biomaterial following the implantation. According to macrophage profile around the XLS/Alg-PAAm hydrogels, M1 macrophages, playing a role in host defense with its destructive phagocytosis ability and secretion of pro-inflammatory cytokines in the early stages of wound healing [58], was observed predominantly (except the first day, $p > 0.05$) due to chronic inflammation at LPS + microenvironment throughout 13 days ($p < 0.0001$). On the other hand, dominant profile of M1 macrophages was observed only on day 1 (M1/M2 ratio was 1.82) at LPS-free microenvironment (Fig. 5A, B).

Fig. 5. Macrophage polarization during 13 days against hydrogels in 3D model of establishing healthy/inflammatory conditions and loading TGF-β3 into the gel. (A) Fluorescence microscopy images of ATDC5, HFOB, L929, Raw264.7 stained for DAPI (blue), M1 surface marker CD80 (green), M2 surface marker CD206 (red). (B) M1/M2 ratio induced by hydrogels during 13 days. ns; $p > 0.05$, *$p < 0.05$, **$p < 0.01$, ****$p < 0.0001$; Two-way ANOVA Tukey's Multiple Comparison Test performed to determine statistically significant differences in cytokine production ($n = 3$ independent experiments). Error bars represent standard deviation. (C) The dot plot graph of qRT-PCR results of M1/M2 gene expressions (CD80, CD68, iNOS, TNF-alpha, CD206, Arg1, STAT6) of cells cultured in the 3D model containing XLS/Alg-PAAm hydrogels. Fold regulation data was shown by dividing the normalized gene expression in each day sample (Day 4, 7, 10, 13) by the normalized gene expression in day 1 sample for all hydrogel groups.

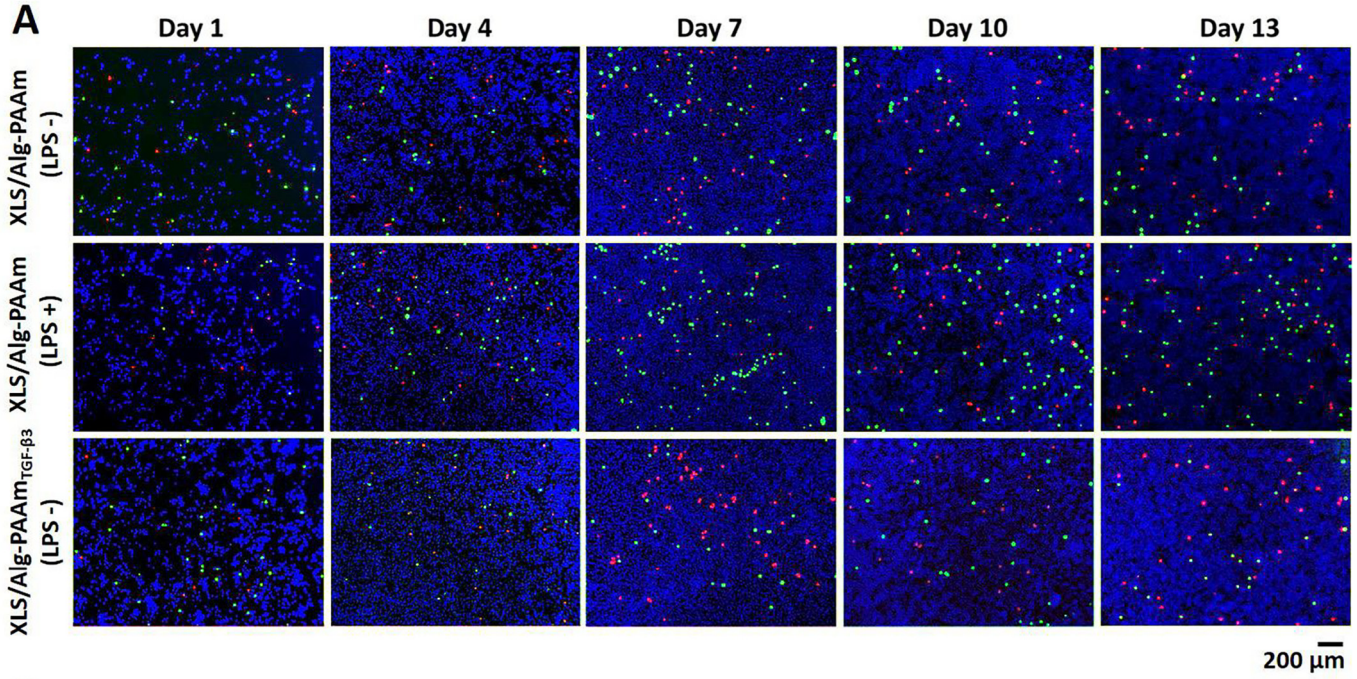
A
Day 1
Day 4
Day 7
Day 10
Day 13
XLS/Alg-PAAm (LPS -)
XLS/Alg-PAAm (LPS +)
XLS/Alg-PAAmTGF-β3 (LPS -)
200 µm

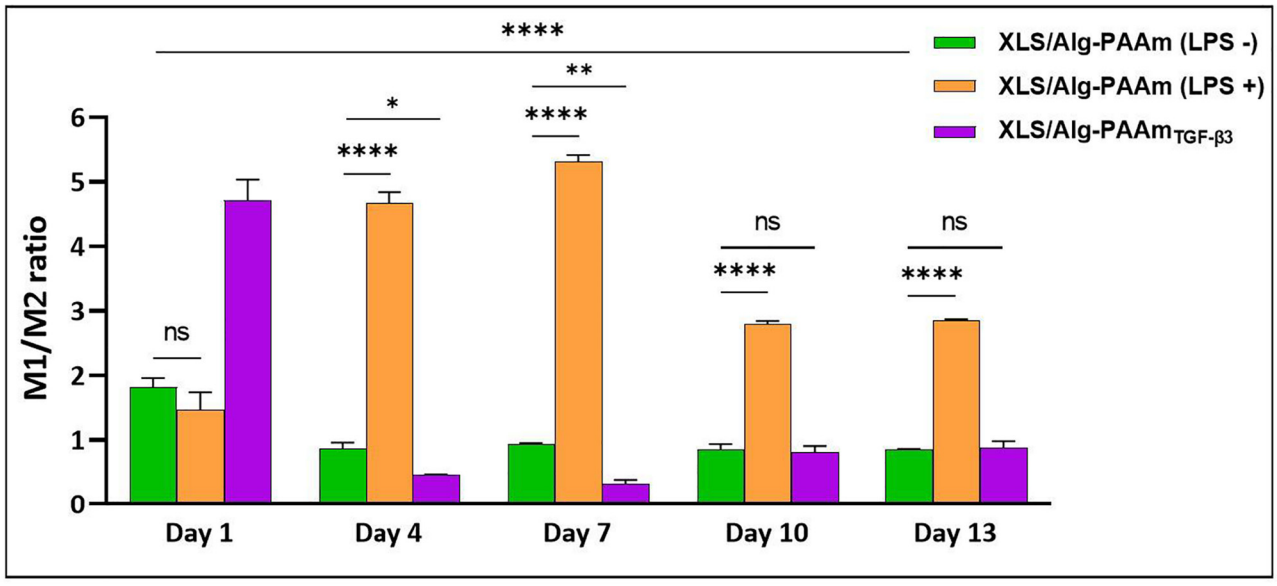
B
M1/M2 ratio
XLS/Alg-PAAm (LPS -)
XLS/Alg-PAAm (LPS +)
XLS/Alg-PAAmTGF-β3
****
**
*
ns
Day 1
Day 4
Day 7
Day 10
Day 13

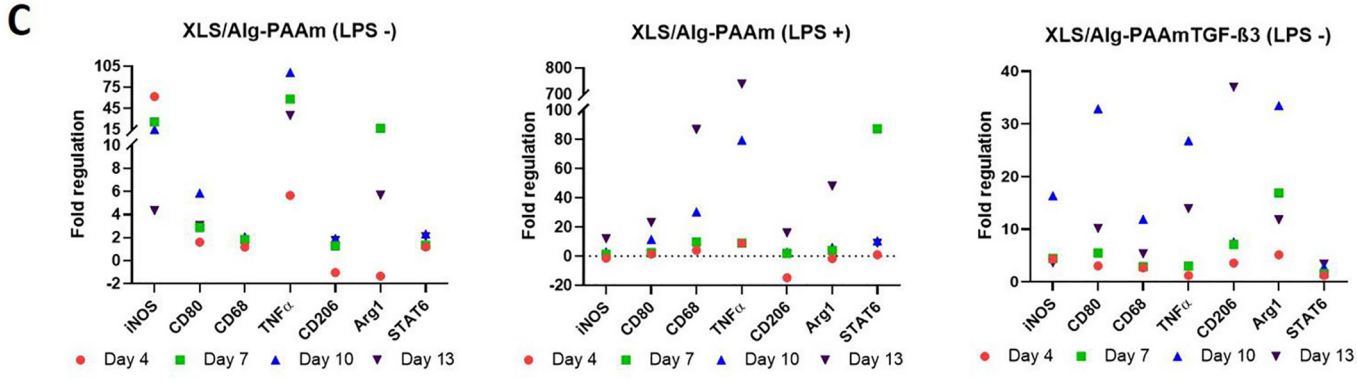
C
XLS/Alg-PAAm (LPS -)
XLS/Alg-PAAm (LPS +)
XLS/Alg-PAAmTGF-ß3 (LPS -)
Fold regulation
iNOS
CD80
CD68
TNFα
CD206
Arg1
STAT6
Day 4
Day 7
Day 10
Day 13

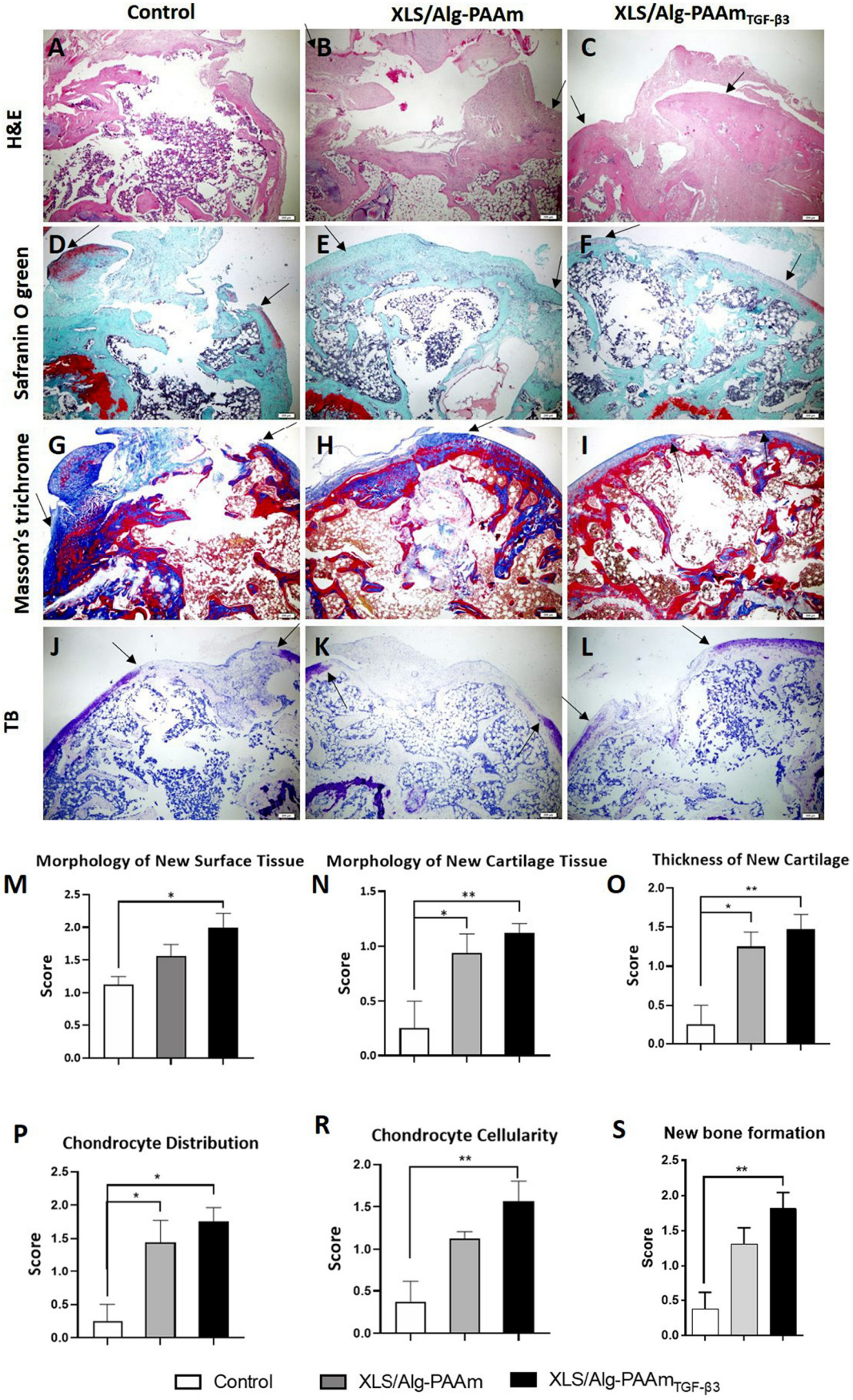
Control
XLS/Alg-PAAm
XLS/Alg-PAAm$_{TGF-\beta3}$
H&E
Safranin O green
Masson's trichrome
TB
A
B
C
D
E
F
G
H
I
J
K
L
M
Morphology of New Surface Tissue
N
Morphology of New Cartilage Tissue
O
Thickness of New Cartilage
P
Chondrocyte Distribution
R
Chondrocyte Cellularity
S
New bone formation
Score
Control
XLS/Alg-PAAm
XLS/Alg-PAAm$_{TGF-\beta3}$

M2 profile became dominant as of day 4 and M1, whereas M2 profiles shifted to a slightly M2 weighted balance on day 13 ($p < 0.0001$) with an M1/M2 ratio of 0.86, attributing to the successful occurrence of damaged tissue repair and constitutive tissue regeneration [59]. Although the biocompatibility and immune response of Alg have been a concern, physicochemical properties such as degree of purity, chemical composition, residues and modifications dictate the degree of biocompatibility and immunogenicity [60]. While M-blocks have been identified as the main initiator of FBR in some studies [61], there was little or no reported immune response to other Alg derivatives, particularly with high purity Alg [62], which is in agreement with our study. Furthermore, it has been reported that high M-block content in Alg provides immunostimulant activity that activates macrophages and monocytes for secretion of cytokines and cytotoxic factors. Also M2 macrophages leading to the secretion of the anti-inflammatory cytokines ensure to attenuate the production of nitric oxide, reactive oxygen species, prostaglandin E2, and cyclooxygenase COX-2, thus indicating the antioxidant effect of Alg [60]. As for the XLS/Alg-PAAm$_{TGF\text{-}\beta3}$ hydrogels, higher M2 presences on day 4 ($p < 0.05$) and 7 ($p < 0.01$) compared to XLS/Alg-PAAm and a slightly more stable M1/M2 ratio (0.88, $p > 0.05$) were observed at the end of day 13. Overall, when the inflammatory microenvironment was induced with LPS, higher M1 polarization with the M1/M2 ratio of 2.85 ($p < 0.0001$) against XLS/Alg-PAAm hydrogel was observed in comparison to the healthy LPS-free microenvironment. Indeed M1 macrophages were shown to induce osteogenesis *via* the cyclooxygenase-2 (COX-2)-prostaglandin E2 (PGE2) pathway during early stages of healing. These results suggest that early initiation of the repair program by M1 macrophages, followed by the transition from M1 to M2 phenotype at the appropriate time point, is key to enhancing bone regeneration [63]. Moreover, several gene expression levels were determined by quantitative qRT-PCR assay to confirm the results of M1 and M2 macrophage polarizations. Gene expressions in all groups were depicted in the dot plot graph based on fold regulation data was provided as well (Fig. 5C, Table S2). The 3D model supported macrophage viabilities as CD68 gene expression indicates the presence of macrophages [64]. The presence of LPS stimulated the gene expressions of CD80, iNOS and TNF-α constantly day by day, upregulating 86.82, 23.1, 11.96 and 739.29-fold at day 13, implying that M1-type macrophages [65] could release destructive factors resulting in cartilage damage. However, the upregulations were comparatively lower in XLS/Alg-PAAm (1.18, 3.05, 4.34 and 34.99-fold) and XLS/Alg-PAAm$_{TGF\text{-}\beta3}$ (5.35, 10.14, 3.63 and 13.93-fold) groups on day 13. On the other hand, CD206 and Arg1 gene expressions increased from 1.75 to 36.97-fold and 5.68 to 11.79-fold in the corresponding TGF-β3 loaded group on day 13, suggesting that XLS/Alg-PAAm$_{TGF\text{-}\beta3}$ further promoted M2 macrophage polarization, which might be associated with accelerated bone repair [66]. Moreover, the gene expression of STAT6, which is an important transcription factor for M2 polarization [67], increased by 2.08 and 3.37-fold at day 13, in the presence of XLS/Alg-PAAm and XLS/Alg-PAAm$_{TGF\text{-}\beta3}$ hydrogels, whereas down-regulated in LPS+ group from day 7 to 13. Overall, the expression levels of M1-related genes were significantly lower in LPS- groups, while the expression levels of M2-related genes were higher than that of LPS+ group. The *in vitro* results indicated that XLS/Alg-PAAm hydrogel activated macrophages towards M2 phenotype and stimulated macrophages to express anti-inflammatory factors. Moreover, TGF-β3 doping seems to enhance the immune response especially between day 4–7 and accelerated the transition of macrophage polarization to the reparative M2 phase compared to XLS/Alg-PAAm suggesting the promoted healing ability.

3.3. In vivo osteochondral defect model

In vivo rat model was used to evaluate the repair of osteochondral defects. All animals revealed normal movement after surgery. Based on macroscopic observations, implants exhibited good integration with host tissue and defects were firmly filled with newly formed tissue in XLS/Alg-PAAm and XLS/Alg-PAAm$_{TGF\text{-}\beta3}$ after 12 weeks. However, the defects in non-treated control group were not fully filled with neotissue with formation of a gap due to adjacent tissue collapse. Additionally, no necrosis, exudation or inflammatory reactions were observed in the joint capsule following implantation at 12 weeks. Histological evaluations of newly formed tissue were confirmed by H&E, Safranin-O/Fast Green, Masson's trichrome, TB (Fig. 6) and PAS staining (Fig. S2) at 12 weeks after surgery. The defects in XLS/Alg-PAAm and XLS/Alg-PAAm$_{TGF\text{-}\beta3}$ demonstrated no inflammation, no collapse of adjacent tissue and completely integrated with the host tissues. XLS/Alg-PAAm and XLS/Alg-PAAm$_{TGF\text{-}\beta3}$ simultaneously enhanced the repair of articular cartilage and subchondral bone in layer fashion, compared to the untreated control. The obtained results were attributed to the osteogenic effect of laponite XLS as well as favorable chondrogenic and osteogenic potencies of TGF-β3. It is well known that the degradation products of laponite XLS enhance bone regeneration by activating Wnt signaling and accelerating collagen type I synthesis [9]. Similarly, XLS/Alg-PAAm group resulted in remarkably enhanced osteochondral regeneration in the absence of any osteoinductive factor compared to non-treated control group. Light microscopic investigations of the articular tissues revealed irregular articular surface with newly formed non-cartilaginous fibrous tissue in the control group (Fig. 6A,D,G,J and Fig. S2A,D,G,J).

XLS/Alg-PAAm group demonstrated disorganized articular surface and the chondral defect was mainly composed of fibrous tissue (Fig. 6B,E,H,K), which can also be seen in magnified photomicrographs of osteochondral tissue sections (Fig. S2B,E,H,K). Few fibrocartilages and hyaline cartilage tissues were observed in some animals. XLS/Alg-PAAm$_{TGF\text{-}\beta3}$ group showed newly formed articular tissue surface, with a fibrocartilage and hyaline cartilage tissue observed in some areas (Fig. 6C,F,I,L and Fig. S2C,F,I,L). Indeed, Alg based hydrogels have been reported to induce macrophage activation and stimulate expression of pro-inflammatory cytokines to accelerate chronic wound healing [68]. The scoring results validated the morphology of new surface (Fig. 6M), cartilage tissues (Fig. 6N) along with the thickness of new cartilage (Fig. 6O) and both distribution (Fig. 6P) and cellularity (Fig. 6R) of chondrocytes. In Masson's trichome staining, blue areas indicates immature nascent bone, while red areas indicates the mature nascent bone [69]. For bone scoring, the white parts in XLS/Alg-PAAm and XLS/Alg-PAAm$_{TGF\text{-}\beta3}$ were observed to decrease in comparison to control in the magnified photomicrographs (Fig. S3). Moreover, blue parts became red mature bone in XLS/Alg-PAAm and XLS/Alg-PAAm$_{TGF\text{-}\beta3}$. Additionally, semiquantitative scoring revealed increased new bone formation in both XLS/Alg-PAAm and XLS/Alg-PAAm$_{TGF\text{-}\beta3}$ ($p < 0.01$) group compared to control group (Fig. 6S). Herein, histological bone scores for non-treated control, XLS/Alg-PAAm and XLS/Alg-PAAm$_{TGF\text{-}\beta3}$ were 0.375, 1.313, and 1.813, respectively. Accordingly, the total histological scores for control, XLS/Alg-PAAm and XLS/Alg-PAAm$_{TGF\text{-}\beta3}$ were determined as 2.625, 7.623, and 9.723 for osteochondral repair. Given the mechanical performance, the stiff bilayer hydrogel described here can find clinical usage for the treatment of osteochondral defects. The major components of XLS/Alg-PAAm are approved for use by the FDA. Furthermore, alginate and polyacrylamide have been used for other clinical applications such as wound dressings (for instance, Algisite M) and fillers for the

Fig. 6. Representative photomicrographs of tissue sections in the experimental groups stained with (A,B,C) H&E, (D,E,F) Safranin O/Fast Green, (G,H,I) Masson's trichrome and (J,K,L) TB stains. (A,D,G,J) Control group demonstrates limited tissue repair mostly composed of fibrous tissue in the chondral region. (B,E,H,K) XLS/Alg-PAAm and (C,F,I,L) XLS/Alg-PAAm$_{TGF\text{-}\beta3}$ groups show mainly fibrous tissue with few fibrocartilage and hyaline cartilage tissue groups in the joint surface (Arrows indicate defect sites). Scale Bars: 200 μm. The histological lesion scores representing the morphology of (M) new surfaces and (N) cartilage tissues along with the (O) tissue thickness, (P) chondrocyte distribution, (R) cellularity as well as (S) new bone formation. ns > 0.05,*$p < 0.05$, **$p < 0.01$; One-Way ANOVA, Tukey's Multiple Comparison Test. Data are presented as the mean ± standard error.

treatment of urinary incontinence [70], highlighting the translational aspect of the fabricated bilayer hydrogel.

4. Conclusions

In the present study, both XLS/Alg-PAAm and XLS/Alg-PAAm$_{TGF-\beta3}$ bilayered hydrogels and their potential to improve the repairment of osteochondral defects were assessed. Having an enhanced mechanical strength, bilayered structures showed appropriate biodegradability with the *in vivo* tissue repairment. As for the foreign body response, although both hydrogels promoted macrophages to polarize towards M2 phenotype, the generated 3D *in vitro* model mimicking the inflammatory state revealed the accelerated transition of macrophage polarization with the addition of TGF-β3, especially between day 4 and 7. Gene expression results also showed that M1-type differentiation was inhibited, whereas M2-type differentiation was promoted. Overall, this study highlights the mechanical and biological functionality of the generated bilayered hydrogel structure through *in vitro* and *in vivo* examinations.

CRediT authorship contribution statement

O.Y.C., J-Y·S., E.A and E.S. conceived the project. Hydrogels synthesize was performed by E.S., P.T. and Y-W·K. Characterization steps were performed by E.S. and E.A. Biocompatibility studies were carried out by E.S., P.S.M. and B.C. Immune responses were evaluated by B.C., P.S.M. and G.B. *In vivo* studies were performed by G.G.E.O.; and K.G. and D.A. participated in the histological examinations. E.S., E.A., B.C., G.B. and P.S.M. wrote the initial manuscript draft, and all authors contributed to the manuscript preparation.

Declaration of competing interest

The authors declare that they have no known competing financial interests or personal relationships that could have appeared to influence the work reported in this paper.

Acknowledgements

This work was supported by The Scientific and Technological Research Council of Turkey (TUBITAK) under grant number 117M843 and immune response studies under grant 219M057. Y.-W.Kim and J.-Y.Sun were supported under the framework of international cooperation program managed by the National Research Foundation of Korea (2017K2A9A1A06037807, FY2017). Authors would like to acknowledge Material Technology Development Program through the National Research Foundation of Korea (NRF) funded by Ministry of Science and ICT (NRF-2018M3A7B4089670). E.S and P.S.M gratefully acknowledge the TUBITAK 2211-A National Graduate Scholarship Program.

Appendix A. Supplementary data

Supplementary data to this article can be found online at https://doi.org/10.1016/j.msec.2022.112721.

References

[1] X. Feng, P. Xu, T. Shen, Y. Zhang, J. Ye, C. Gao, Age-related regeneration of osteochondral and tibial defects by a fibrin-based construct in vivo, Front. Bioeng. Biotechnol. 8 (2020) 404, https://doi.org/10.3389/fbioe.2020.00404.
[2] P.B. Malafaya, R.L. Reis, Bilayered chitosan-based scaffolds for osteochondral tissue engineering: influence of hydroxyapatite on in vitro cytotoxicity and dynamic bioactivity studies in a specific double-chamber bioreactor, Acta Biomater. 5 (2009) 644–660, https://doi.org/10.1016/j.actbio.2008.09.017.
[3] X. Chen, M. Wang, F. Chen, J. Wang, X. Li, J. Liang, Y. Fan, Y. Xiao, X. Zhang, Correlations between macrophage polarization and osteoinduction of porous calcium phosphate ceramics, Acta Biomater. 103 (2020) 318–332, https://doi.org/10.1016/j.actbio.2019.12.019.
[4] N. Chauhan, P. Gupta, L. Arora, D. Pal, Y. Singh, Dexamethasone-loaded, injectable pullulan-Poly(ethylene glycol) hydrogels for bone tissue regeneration in chronic inflammatory conditions, Mater. Sci. Eng. C. (2021), 112463, https://doi.org/10.1016/J.MSEC.2021.112463.
[5] K. Kaur, S.S. Paiva, D. Caffrey, B.L. Cavanagh, C.M. Murphy, Injectable chitosan/collagen hydrogels nano-engineered with functionalized single wall carbon nanotubes for minimally invasive applications in bone, Mater. Sci. Eng. C. 128 (2021), 112340, https://doi.org/10.1016/J.MSEC.2021.112340.
[6] J. Liao, T. Tian, S. Shi, X. Xie, Q. Ma, G. Li, Y. Lin, The fabrication of biomimetic biphasic CAN-PAC hydrogel with a seamless interfacial layer applied in osteochondral defect repair, Bone Res. 5 (2017) 1–15, https://doi.org/10.1038/boneres.2017.18.
[7] M. Nowicki, W. Zhu, K. Sarkar, R. Rao, L.G. Zhang, 3D printing multiphasic osteochondral tissue constructs with nano to micro features via PCL based bioink, Bioprinting 17 (2020), e00066, https://doi.org/10.1016/j.bprint.2019.e00066.
[8] G. Cidonio, M. Cooke, M. Glinka, J.I. Dawson, L. Grover, R.O.C. Oreffo, Printing bone in a gel: using nanocomposite bioink to print functionalised bone scaffolds, Mater. Today Bio. 4 (2019), 100028, https://doi.org/10.1016/j.mtbio.2019.100028.
[9] A.K. Gaharwar, S.M. Mihaila, A. Swami, A. Patel, S. Sant, R.L. Reis, A.P. Marques, M.E. Gomes, A. Khademhosseini, Bioactive silicate nanoplatelets for osteogenic differentiation of human mesenchymal stem cells, Adv. Mater. 25 (2013) 3329–3336, https://doi.org/10.1002/adma.201300584.
[10] J. Park, M. Kim, S. Choi, J.Y. Sun, Self-healable soft shield for γ-ray radiation based on polyacrylamide hydrogel composites, Sci. Rep. 10 (2020) 1–8, https://doi.org/10.1038/s41598-020-78663-x.
[11] F. Afghah, M. Altunbek, C. Dikyol, B. Koc, Preparation and characterization of nanoclay-hydrogel composite support-bath for bioprinting of complex structures, Sci. Rep. 10 (2020) 1–13, https://doi.org/10.1038/s41598-020-61606-x.
[12] N. Golafshan, R. Rezahasani, M. Tarkesh Esfahani, M. Kharaziha, S.N. Khorasani, Nanohybrid hydrogels of laponite: PVA-alginate as a potential wound healing material, Carbohydr. Polym. 176 (2017) 392–401, https://doi.org/10.1016/j.carbpol.2017.08.070.
[13] ISO, ISO 10993-12:2012 - biological evaluation of medical devices — Part 12: sample preparation and reference materials, (n.d.) https://www.iso.org/standard/53468.html (accessed July 7, 2021).
[14] ISO, ISO 10993-5:2009 - Biological evaluation of medical devices — part 5: tests for in vitro cytotoxicity, (n.d.) https://www.iso.org/standard/36406.html (accessed May 10, 2020).
[15] E. Ilhan-Ayisigi, F. Ulucan, E. Saygili, P. Saglam-Metiner, S. Gulce-Iz, O. Yesil-Celiktas, Nano-vesicular formulation of propolis and cytotoxic effects in a 3D spheroid model of lung cancer, J. Sci. Food Agric. 100 (2020) 3525–3535, https://doi.org/10.1002/jsfa.10400.
[16] D. Xue, Q. Zheng, C. Zong, Q. Li, H. Li, S. Qian, B. Zhang, L. Yu, Z. Pan, Osteochondral repair using porous poly(lactide-co-glycolide)/ nano-hydroxyapatite hybrid scaffolds with undifferentiated mesenchymal stem cells in a rat model, J. Biomed. Mater. Res. A 94 (2010) 259–270, https://doi.org/10.1002/jbm.a.32691.
[17] T.A. Holland, E.W.H. Bodde, V.M.J.I. Cuijpers, L.S. Baggett, Y. Tabata, A.G. Mikos, J.A. Jansen, Degradable hydrogel scaffolds for in vivo delivery of single and dual growth factors in cartilage repair, Osteoarthr. Cartil. 15 (2007) 187–197, https://doi.org/10.1016/j.joca.2006.07.006.
[18] Y.W. Chen, M.Y. Chen, D.J. Hsieh, S. Periasamy, K.C. Yen, C.T. Chuang, H.C. Wang, F.W. Tseng, J.C. Kuo, H.H. Chien, Evaluating the bone-regenerative role of the decellularized porcine bone xenograft in a canine extraction socket model, Clin. Exp. Dent. Res. 7 (2021) 409–418, https://doi.org/10.1002/cre2.361.
[19] E. Saygili, E. Kaya, E. Ilhan-Ayisigi, P. Saglam-Metiner, E. Alarcin, A. Kazan, E. Girgic, Y.W. Kim, K. Gunes, G.G. Eren-Ozcan, D. Akakin, J.Y. Sun, O. Yesil-Celiktas, An alginate-poly(acrylamide) hydrogel with TGF-β3 loaded nanoparticles for cartilage repair: biodegradability, biocompatibility and protein adsorption, Int. J. Biol. Macromol. 172 (2021) 381–393, https://doi.org/10.1016/J.IJBIOMAC.2021.01.069.
[20] J.L. Drury, D.J. Mooney, Hydrogels for tissue engineering: scaffold design variables and applications, Biomaterials 24 (2003) 4337–4351, https://doi.org/10.1016/S0142-9612(03)00340-5.
[21] A. Eftekhari, S.M. Dizaj, S. Sharifi, S. Salatin, Y.R. Saadat, S.Z. Vahed, M. Samiei, M. Ardalan, M. Rameshrad, E. Ahmadian, M. Cucchiarini, The use of nanomaterials in tissue engineering for cartilage regeneration; current approaches and future perspectives, Int. J. Mol. Sci. 21 (2020)https://doi.org/10.3390/ijms21020536.
[22] C.Z. Jin, J.H. Cho, B.H. Choi, L.M. Wang, M.S. Kim, S.R. Park, J.H. Yun, H.J. Oh, B.H. Min, The maturity of tissue-engineered cartilage in vitro affects the repairability for osteochondral defect, Tissue Eng. A 17 (2011) 3057–3065, https://doi.org/10.1089/ten.tea.2010.0605.
[23] B. Liu, J. Li, X. Lei, S. Miao, S. Zhang, P. Cheng, Y. Song, H. Wu, Y. Gao, L. Bi, G. Pei, Cell-loaded injectable gelatin/alginate/LAPONITE® nanocomposite hydrogel promotes bone healing in a critical-size rat calvarial defect model, RSC Adv. 10 (2020) 25652–25661, https://doi.org/10.1039/d0ra03040f.
[24] M. Ghadiri, W. Chrzanowski, W.H. Lee, A. Fathi, F. Dehghani, R. Rohanizadeh, Physicochemical, mechanical and cytotoxicity characterizations of Laponite®/alginate nanocomposite, Appl. Clay Sci. 85 (2013) 64–73, https://doi.org/10.1016/j.clay.2013.08.049.
[25] X. Zhai, Y. Ma, C. Hou, F. Gao, Y. Zhang, C. Ruan, H. Pan, W.W. Lu, W. Liu, 3D-Printed High Strength Bioactive Supramolecular Polymer / Clay Nanocomposite Hydrogel Sca ff old for Bone Regeneration, 2017, https://doi.org/10.1021/acsbiomaterials.7b00224.
[26] B. Liu, Y. Zhao, T. Zhu, S. Gao, K. Ye, F. Zhou, D. Qiu, X. Wang, Y. Tian, X. Qu, Biphasic double-network hydrogel with compartmentalized loading of bioactive glass for osteochondral defect repair, Front. Bioeng. Biotechnol. 8 (2020) 752, https://doi.org/10.3389/fbioe.2020.00752.
[27] J.L. Dávila, M.A. D'Ávila, Rheological evaluation of Laponite/alginate inks for 3D extrusion-based printing, Int. J. Adv. Manuf. Technol. 101 (2019) 675–686, https://doi.org/10.1007/s00170-018-2876-y.

[28] J.Y. Sun, X. Zhao, W.R.K. Illeperuma, O. Chaudhuri, K.H. Oh, D.J. Mooney, J.J. Vlassak, Z. Suo, Highly stretchable and tough hydrogels, Nature 489 (2012) 133–136, https://doi.org/10.1038/nature11409.

[29] P. Li, N.H. Siddaramaiah, S.B. Kim, J.H. Heo, Lee, novel PAAm/Laponite clay nanocomposite hydrogels with improved cationic dye adsorption behavior, Compos. Part B 39 (2008) 756–763, https://doi.org/10.1016/j.compositesb.2007.11.003.

[30] A. Vishwakarma, N.S. Bhise, M.B. Evangelista, J. Rouwkema, M.R. Dokmeci, A.M. Ghaemmaghami, N.E. Vrana, A. Khademhosseini, Engineering immunomodulatory biomaterials to tune the inflammatory response, Trends Biotechnol. 34 (2016) 470–482, https://doi.org/10.1016/j.tibtech.2016.03.009.

[31] J. Naranda, M. Braˇ, Recent Advancements in 3D Printing of Polysaccharide Hydrogels in Cartilage Tissue Engineering, 2021.

[32] G. Ge, J. Bai, Q. Wang, X. Liang, H. Tao, H. Chen, Punicalagin Ameliorates Collagen-induced Arthritis by Downregulating M1 Macrophage and Pyroptosis via NF-κB Signaling Pathway 2021, pp. 1–16.

[33] R. Zeng, X. Lu, J. Lin, Z. Ron, J. Fang, Z. Liu, W. Zeng, FOXM1 activates JAK1/STAT3 pathway in human osteoarthritis cartilage cell inflammatory reaction, Exp. Biol. Med. 246 (2021) 644–653, https://doi.org/10.1177/1535370220974933.

[34] Y.P. Singh, J.C. Moses, N. Bhardwaj, B.B. Mandal, Overcoming the dependence on animal models for osteoarthritis therapeutics – the promises and prospects of in vitro models, Adv. Healthc. Mater. 10 (2021), https://doi.org/10.1002/adhm.202100961.

[35] Z. Zheng, Y. Chen, H. Hong, Y. Shen, Y. Wang, J. Sun, X. Wang, The "Yin and Yang" of immunomodulatory magnesium-enriched graphene oxide nanoscrolls decorated biomimetic scaffolds in promoting bone regeneration, Adv. Healthc. Mater. 10 (2021) 1–14, https://doi.org/10.1002/adhm.202000631.

[36] F. Sharifi, S.S. Htwe, M. Righi, H. Liu, A. Pietralunga, O. Yesil-Celiktas, S. Maharjan, B.-H. Cha, S.R. Shin, M.R. Dokmeci, N.E. Vrana, A.M. Ghaemmaghami, A. Khademhosseini, Y.S. Zhang, A foreign body response-on-a-Chip platform, Adv. Healthc. Mater. 8 (2019), 1801425, https://doi.org/10.1002/adhm.201801425.

[37] J. Jia, J. Wang, J. Zhang, M. Cui, X. Sun, Q. Li, B. Zhao, MiR-125b inhibits LPS-induced inflammatory injury via targeting MIP-1α in chondrogenic cell ATDC5, Cell. Physiol. Biochem. 45 (2018) 2305–2316, https://doi.org/10.1159/000488178.

[38] G. Zhou, T. Groth, Host responses to biomaterials and anti-inflammatory design—a brief review, Macromol. Biosci. 18 (2018) 1–15, https://doi.org/10.1002/mabi.201800112.

[39] C.E. Witherel, D. Abebayehu, T.H. Barker, K.L. Spiller, Macrophage and fibroblast interactions in biomaterial-mediated fibrosis, Adv. Healthc. Mater. 8 (2019) 1–16, https://doi.org/10.1002/adhm.201801451.

[40] N. Fahy, E. Farrell, T. Ritter, A.E. Ryan, J.M. Murphy, Immune modulation to improve tissue engineering outcomes for cartilage repair in the osteoarthritic joint, Tissue Eng. B Rev. 21 (2014) 55–66, https://doi.org/10.1089/ten.teb.2014.0098.

[41] A.D. Gilmour, A.J. Woolley, L.A. Poole-Warren, C.E. Thomson, R.A. Green, A critical review of cell culture strategies for modelling intracortical brain implant material reactions, Biomaterials 91 (2016) 23–43, https://doi.org/10.1016/j.biomaterials.2016.03.011.

[42] L. Chen, L. Zhang, H. Zhang, X. Sun, D. Liu, J. Zhang, Y. Zhang, L. Cheng, H.A. Santos, W. Cui, Programmable immune activating electrospun fibers for skin regeneration, Bioact. Mater. 6 (2021) 3218–3230, https://doi.org/10.1016/j.bioactmat.2021.02.022.

[43] C. Montoya, Y. Du, A.L. Gianforcaro, S. Orrego, M. Yang, P.I. Lelkes, On the road to smart biomaterials for bone research: definitions, concepts, advances, and outlook, Bone Res. 9 (2021), https://doi.org/10.1038/s41413-020-00131-z.

[44] J. Anderson, S. Cramer, Perspectives on the Inflammatory, Healing, and Foreign Body Responses to Biomaterials and Medical Devices, Elsevier Inc, 2015, https://doi.org/10.1016/B978-0-12-800196-7.00002-5.

[45] M. Li, H. Yin, Z. Yan, H. Li, J. Wu, Y. Wang, F. Wei, G. Tian, C. Ning, H. Li, C. Gao, L. Fu, S. Jiang, M. Chen, X. Sui, S. Liu, Z. Chen, Q. Guo, The immune microenvironment in cartilage injury and repair, Acta Biomater. (2021), https://doi.org/10.1016/j.actbio.2021.12.006.

[46] Y. Xie, C. Hu, Y. Feng, D. Li, T. Ai, Y. Huang, X. Chen, L. Huang, J. Tan, Osteoimmunomodulatory effects of biomaterial modification strategies on macrophage polarization and bone regeneration, Regen. Biomater. 7 (2020) 233–245, https://doi.org/10.1093/rb/rbaa006.

[47] R. Sridharan, A.R. Cameron, D.J. Kelly, C.J. Kearney, F.J. O'Brien, Biomaterial based modulation of macrophage polarization: a review and suggested design principles, Mater. Today 18 (2015) 313–325, https://doi.org/10.1016/j.mattod.2015.01.019.

[48] Y. Zhu, S. Deng, Z. Ma, L. Kong, H. Li, H.F. Chan, Macrophages activated by akermanite/alginate composite hydrogel stimulate migration of bone marrow-derived mesenchymal stem cells, Biomed. Mater. 16 (2021) https://doi.org/10.1088/1748-605X/abe80a.

[49] Z. Chen, A. Bozec, A. Ramming, G. Schett, Anti-inflammatory and immune-regulatory cytokines in rheumatoid arthritis, Nat. Rev. Rheumatol. 15 (2019) 9–17, https://doi.org/10.1038/s41584-018-0109-2.

[50] B.H. Cha, S.R. Shin, J. Leijten, Y.C. Li, S. Singh, J.C. Liu, N. Annabi, R. Abdi, M.R. Dokmeci, N.E. Vrana, A.M. Ghaemmaghami, A. Khademhosseini, Integrin-mediated interactions control macrophage polarization in 3D hydrogels, Adv. Healthc. Mater. 6 (2017) 1–12, https://doi.org/10.1002/adhm.201700289.

[51] Y. Deng, A.X. Sun, K.J. Overholt, G.Z. Yu, M.R. Fritch, P.G. Alexander, H. Shen, R.S. Tuan, H. Lin, Enhancing chondrogenesis and mechanical strength retention in physiologically relevant hydrogels with incorporation of hyaluronic acid and direct loading of TGF-β, Acta Biomater. 83 (2019) 167–176, https://doi.org/10.1016/J.ACTBIO.2018.11.022.

[52] M. Qasim, N.X.T. Le, T.P.T. Nguyen, D.S. Chae, S.J. Park, N.Y. Lee, Nanohybrid biodegradable scaffolds for TGF-β3 release for the chondrogenic differentiation of human mesenchymal stem cells, Int. J. Pharm. 581 (2020), 119248, https://doi.org/10.1016/J.IJPHARM.2020.119248.

[53] J. Sikora, M. Smycz-Kubańska, A. Mielczarek-Palacz, I. Bednarek, Z. Kondera-Anasz, The involvement of multifunctional TGF-β and related cytokines in pathogenesis of endometriosis, Immunol. Lett. 201 (2018) 31–37, https://doi.org/10.1016/J.IMLET.2018.10.011.

[54] T. Baroni, P. Carinci, C. Bellucci, C. Lilli, E. Becchetti, F. Carinci, G. Stabellini, F. Pezzetti, E. Caramelli, M. Tognon, M. Bodo, Cross-talk between Interleukin-6 and transforming growth factor-β3 regulates extracellular matrix production by human fibroblasts from subjects with non-syndromic cleft lip and palate, J. Periodontol. 74 (2003) 1447–1453, https://doi.org/10.1902/JOP.2003.74.10.1447.

[55] D.J. Sharkey, A.M. Macpherson, K.P. Tremellen, D.G. Mottershead, R.B. Gilchrist, S.A. Robertson, TGF-β mediates proinflammatory seminal fluid signaling in human cervical epithelial cells, J. Immunol. 189 (2012) 1024–1035, https://doi.org/10.4049/JIMMUNOL.1200005.

[56] M. Kondo, K. Yamaoka, K. Sakata, K. Sonomoto, L. Lin, K. Nakano, Y. Tanaka, Contribution of the interleukin-6/STAT-3 signaling pathway to chondrogenic differentiation of human mesenchymal stem cells, Arthritis Rheumatol. 67 (2015) 1250–1260, https://doi.org/10.1002/ART.39036.

[57] L. Parisi, E. Gini, D. Baci, M. Tremolati, M. Fanuli, B. Bassani, G. Farronato, A. Bruno, L. Mortara, Macrophage polarization in chronic inflammatory diseases: killers or builders? J Immunol Res 2018 (2018), https://doi.org/10.1155/2018/8917804.

[58] A. Ibáñez-Fonseca, S. Santiago Maniega, D. Gorbenko del Blanco, B. Catalán Bernardos, A. Vega Castrillo, Á.J. Álvarez Barcia, M. Alonso, H.J. Aguado, J.C. Rodríguez-Cabello, Elastin-like recombinamer hydrogels for improved skeletal muscle healing through modulation of macrophage polarization, Front. Bioeng. Biotechnol. 8 (2020) 1–12, https://doi.org/10.3389/fbioe.2020.00413.

[59] K.E. Martin, A.J. García, Macrophage phenotypes in tissue repair and the foreign body response: implications for biomaterial-based regenerative medicine strategies, Acta Biomater. (2021), https://doi.org/10.1016/j.actbio.2021.03.038.

[60] G. Cattelan, A.Guerrero Gerbolés, R. Foresti, P.P. Pramstaller, A. Rossini, M. Miragoli, C. Caffarra Malvezzi, Alginate formulations: current developments in the race for hydrogel-based cardiac regeneration, Front. Bioeng. Biotechnol. 8 (2020), https://doi.org/10.3389/fbioe.2020.00414.

[61] M. Rezaa Mohammadi, S. Rodrigez, R. Cao, M. Alexander, J.R.T. Lakey, Immune response to subcutaneous implants of alginate microcapsules, Mater. Today Proc. 5 (2018) 15580–15585, https://doi.org/10.1016/j.matpr.2018.04.166.

[62] G. Orive, S. Ponce, R.M. Hernández, A.R. Gascón, M. Igartua, J.L. Pedraz, Biocompatibility of microcapsules for cell immobilization elaborated with different type of alginates, Biomaterials 23 (2002) 3825–3831, https://doi.org/10.1016/S0142-9612(02)00118-7.

[63] L.Y. Lu, F. Loi, K. Nathan, T.H. Lin, J. Pajarinen, E. Gibon, A. Nabeshima, L. Cordova, E. Jämsen, Z. Yao, S.B. Goodman, Pro-inflammatory M1 macrophages promote osteogenesis by mesenchymal stem cells via the COX-2-prostaglandin E2 pathway, J. Orthop. Res. 35 (2017) 2378–2385, https://doi.org/10.1002/jor.23553.

[64] H. Li, J. Sun, H. Yang, X. Han, X. Luo, L.J. Liao, B. Yang, T. Zhu, F. Huo, W. Guo, W. Tian, Recruited CD68 + CD206 + macrophages orchestrate graft immune tolerance to prompt xenogeneic-dentin matrix-based tooth root regeneration, Bioact. Mater. 6 (2021) 1051–1072, https://doi.org/10.1016/j.bioactmat.2020.09.029.

[65] G. Jiang, S. Li, K. Yu, B. He, J. Hong, T. Xu, J. Meng, C. Ye, Y. Chen, Z. Shi, G. Feng, W. Chen, S. Yan, Y. He, R. Yan, A 3D-printed PRP-GelMA hydrogel promotes osteochondral regeneration through M2 macrophage polarization in a rabbit model, Acta Biomater. 128 (2021) 150–162, https://doi.org/10.1016/j.actbio.2021.04.010.

[66] J. Sun, L. Li, F. Xing, Y. Yang, M. Gong, G. Liu, S. Wu, R. Luo, X. Duan, M. Liu, M. Zou, Z. Xiang, Graphene oxide-modified silk fibroin/nanohydroxyapatite scaffold loaded with urine-derived stem cells for immunomodulation and bone regeneration, Stem Cell Res Ther 12 (2021) 1–20, https://doi.org/10.1186/s13287-021-02634-w.

[67] F. Zhou, J. Mei, X. Han, H. Li, S. Yang, M. Wang, L. Chu, H. Qiao, T. Tang, Kinsenoside attenuates osteoarthritis by repolarizing macrophages through inactivating NF-κB/MAPK signaling and protecting chondrocytes, Acta Pharm. Sin. B 9 (2019) 973–985, https://doi.org/10.1016/j.apsb.2019.01.015.

[68] H. Zhang, J. Cheng, Q. Ao, Preparation of alginate-based biomaterials and their applications in biomedicine, Mar. Drugs 19 (2021) 1–24, https://doi.org/10.3390/md19050264.

[69] S. Wang, Y. Yang, G.L. Koons, A.G. Mikos, Z. Qiu, T. Song, F. Cui, X. Wang, Tuning pore features of mineralized collagen/PCL scaffolds for cranial bone regeneration in a rat model, Mater. Sci. Eng. C. 106 (2020), 110186, https://doi.org/10.1016/j.msec.2019.110186.

[70] A.D. Kasi, V. Pergialiotis, D.N. Perrea, A. Khunda, S.K. Doumouchtsis, Polyacrylamide hydrogel (Bulkamid®) for stress urinary incontinence in women: a systematic review of the literature, Int. Urogynecol. J. 27 (2016) 367–375, https://doi.org/10.1007/s00192-015-2781-y.